Symposium on Materials Science

Mátraháza, Hungary, September 24-26, 2025

Editor:
Miklós Fried
Department of Microelectronics and Technology, Óbuda University
2026

ISBN 978-963-449-415-7

Organizing and Programme Committee:

Miklós Fried (editor, Department of Microelectronics and Technology, Óbuda University)

Ákos Nemcsics (Department of Microelectronics and Technology, Óbuda University)

Attila Bonyár (Department of Materials Science and Engineering, Budapest University of Technology and Economics)

Péter Petrik (Institute of Technical Physics and Material Science, Centre for Energy Research)

András Deák (Institute of Technical Physics and Material Science, Centre for Energy Research)

ISBN 978-963-449-415-7

Table of contents

The Symposium

Lecturer: Dániel Zámbó Lecturer: András Deák

Lecturer: Géza Szántó Lecturer: Dániel Olasz


Lecturer: Anita Horváth

Lecturer: Bálint Medgyes


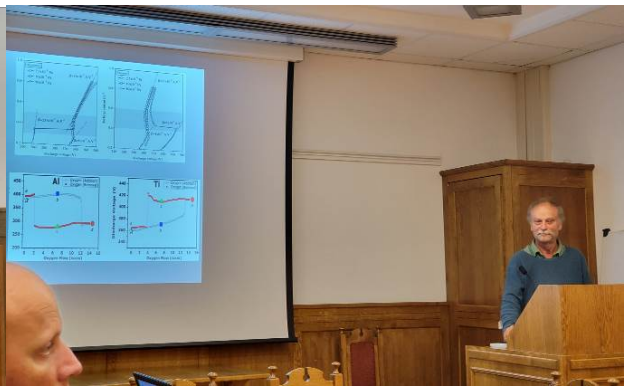

Lecturer: Dávid Kovács

Lecturer: György Sáfrán

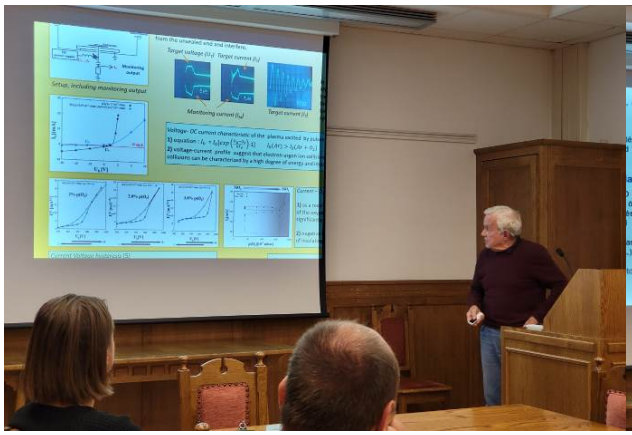
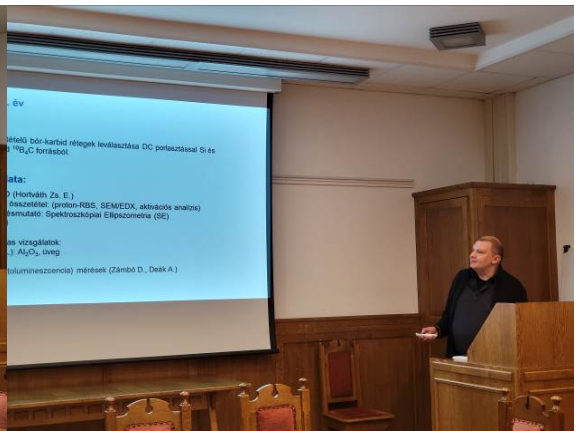

Lecturer: Miklós Serényi

Lecturer: Zsolt Zolnai

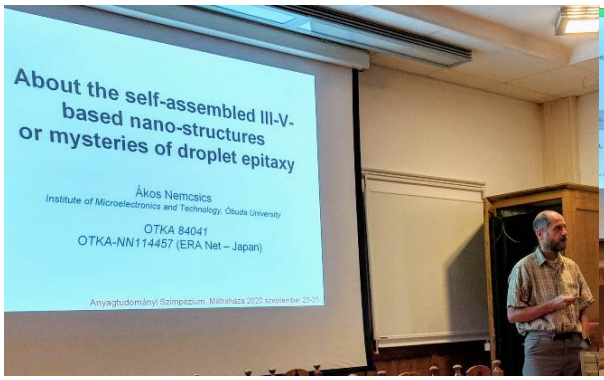

Lecturer: Ákos Nemcsics

Lecturer: Marcell Gajdics

Lecturer: Miklós Fried

Lecturer: Péter Petrik

Gold nanoparticle–assisted electrochemical immobilization of proteins for heavy–metal ion sensing

Máté Kálmán Stift[1,2], Attila Bonyár[2], Zoltán Lábadi[3], Hajnalka Jankovics[4], Ferenc Vonderviszt[5], Péter Petrik[6]

[1]HUN-REN Centre for Energy Research, Institute of Technical Physics and Materials Science,
stift.mate@ek.hun-ren.hu
1121 Budapest, Konkoly-Thege Miklós út 29–33.

[2]Budapest University of Technology and Economics, Faculty of Electrical Engineering and Informatics, Department of Electronics Technology, bonyar.attila@vik.bme.hu
1111 Budapest, Egry József utca 18.

[3]HUN-REN Centre for Energy Research, Institute of Technical Physics and Materials Science,
labadi.zoltan@ek.hun-ren.hu
1121 Budapest, Konkoly-Thege Miklós út 29–33.

[4]Research Institute of Biomolecular and Chemical Engineering, University of Pannonia,
jankovics.hajnalka@mk.uni-pannon.hu
8200 Veszprém, Egyetem utca 10.

[5]Research Institute of Biomolecular and Chemical Engineering, University of Pannonia,
vonderviszt.ferenc@mk.uni-pannon.hu
8200 Veszprém, Egyetem utca 10.

[6]HUN-REN Centre for Energy Research, Institute of Technical Physics and Materials Science,
petrik.peter@ek.hun-ren.hu
1121 Budapest, Konkoly-Thege Miklós út 29–33.

Abstract. Gold nanoparticle (AuNP) layers on gold–evaporated silicon samples enable both optical and electrochemical sensing of dissolved contaminants. We outline a practical route to form AuNP–covered films by chronoamperometry (CA) and to immobilize bioengineered protein filaments for selective heavy– metal binding. Real–time spectroscopic ellipsometry (SE/SPR–SE) monitors layer growth during CA and subsequent protein attachment, while cyclic voltammetry (CV) shows concentration–dependent redox responses. The approach aims at a portable, independent water testing sensor with improved sensitivity over colorimetric strips.

Keywords: heavy metal sensing, ellipsometry, electrochemistry, gold nanoparticles, sensor protein

Introduction

Table 1: WHO limits for selected heavy–metal ions in drinking water, and their primary health risks [1].

Ion	Limit (mg/L)	Main health risks
Ni(II)	0.07	cancer, allergic reactions
Cu(II)	2.00	anaemia, kidney disease
Zn(II)	3.00	respiratory and neurological disorders, prostate cancer
Fe(III)	0.30	haemochromatosis, liver and heart damage
As(III)	0.005	CNS damage; cardiovascular, pulmonary, dermatological and gastrointestinal diseases
Cr(VI)	0.10	embryotoxicity, reproductive toxicity, mutagenicity, carcinogenicity, skin problems

Heavy–metal contamination of drinking water is a global health problem, especially in the underdeveloped countries. The guideline values in Table 1 define the concentration range in which a practical sensor must operate and motivate the development of methods capable of ppm–level detection.

Colorimetric test kits (e.g. for arsenic) allow rapid on–site measurements, but the readout is visual and strongly user–dependent: the operator must compare the strip colour against a reference chart, and weak colour changes are difficult to interpret reproducibly [1].

Figure 1: Example of a rapid arsenic test kit for drinking water analysis [2].

There is a clear motivation to develop such portable sensors that provide quantitative signals instead of rather subjective colour changes. In this work we propose a hybrid optical–electrochemical approach based on AuNP–covered samples and protein layers. The long–term goal is a field–deployable heavy–metal sensor, primarily for Ni(II), that does not require specialized workforce to evaluate at the sampling site [3, 4].

Materials and methods

Gold–evaporated silicon samples

Gold–evaporated silicon samples are used as starting substrates for the sensor development workflow. Their surface quality and dimensions are compatible with both ellipsometry and electrochemistry, and several deposition spots can be prepared on the same sample if needed.

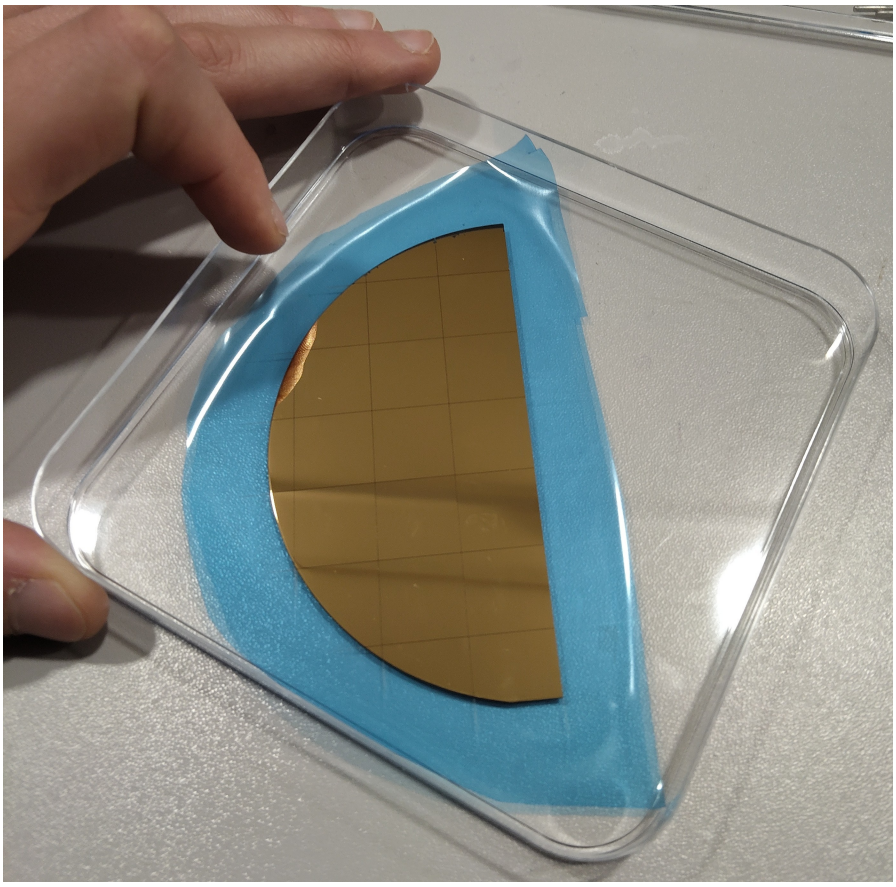

Figure 2: Gold–evaporated silicon samples – the starting point of the sensor development project.

Process flow

First, a thin gold layer is nanostructured by depositing AuNP onto the surface using electrochemical methods. This AuNP layer increases the specific surface area and provides adequate chemistry for binding the sensor protein layer.

In the second step, modified sensor protein filaments produced at the University of Pannonia are immobilised on the AuNP layer. The proteins are dissolved in 0.1 M HEPES buffer (pH = 7.1) and attached to the surface by preparative CV over a small number of cycles. Previous experiments and literature show that most binding takes place in the initial cycles [3, 4]. Owing to their side chains, these filaments enable voltammetric detection of heavy–metal ions, especially Ni(II), in the relevant concentration range.

Both the AuNP layer and the protein layer are formed electrochemically (CA and CV), while

their growth is monitored optically in real time by ellipsometry.

Electrochemical methods

AuNP deposition. AuNP decoration is carried out on the gold–evaporated samples from an aqueous $HAuCl_4$ solution. A 5.14 mM solution is prepared and diluted to working concentrations (for example 2 mM) depending on the targeted morphology. The goal is to increase specific surface area and to promote protein binding to the surface.

Chronoamperometry (CA) and cyclic voltammetry (CV) are the two main techniques. In CA, potential steps selected from a prior CV map (e.g. between −1.0 and +0.3 V vs. reference) promote nucleation followed by growth. The diffusion–limited current follows the Cottrell law

$$i(t) = nFAC_0\ \overline{sqrt}(D/\pi t) \quad (1)$$

where n is the number of electrons, F the Faraday constant, A the electrode area, C_0 the bulk concentration and D the diffusion coefficient.

Cyclic voltammetry. For both deposition and sensing, the key diagnostic is CV [5, 6]. In CV the electrode potential is swept linearly in time, and the resulting current–potential curve (voltammogram) reveals redox processes for the user. Peak positions inform on thermodynamics, while peak areas and their scan–rate dependence provide kinetic and mass–transport information.

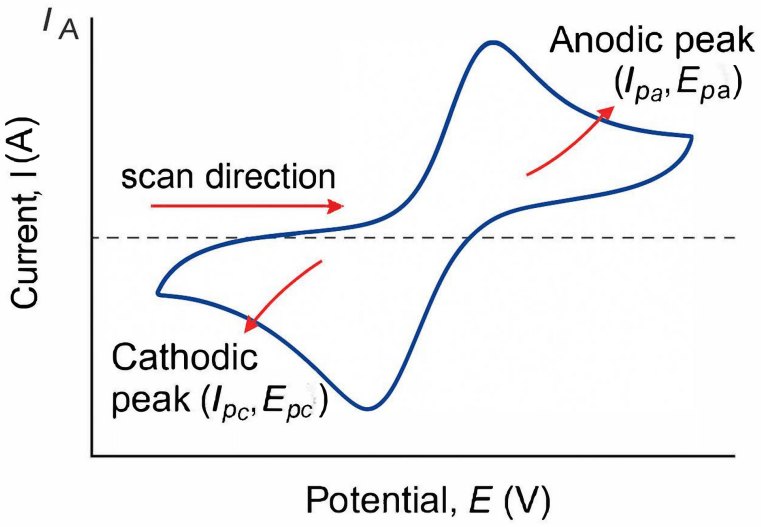

Figure 3: Schematic shape of a typical cyclic voltammogram with anodic and cathodic peaks [5].

The potential window, scan rate (time derivative of the applied voltage) and number of cycles must be chosen carefully. If the window is too narrow or the scanning is too slow we may lose useful redox information. Moreover, too aggressive conditions can damage the protein layer or drive unwanted side reactions. In the preparative protocol most immobilization takes place during the first few cycles, after which the voltammogram stabilizes.

Spectroscopic ellipsometry

Spectroscopic ellipsometry (SE) is used as a non–destructive, highly sensitive, in situ monitor of nm–scale changes during AuNP formation and protein binding [7]. For nanotechnology applications it fulfills the most important requirements: it is non–invasive, relatively low–cost per measurement, fast, and does not require any complex sample preparation.

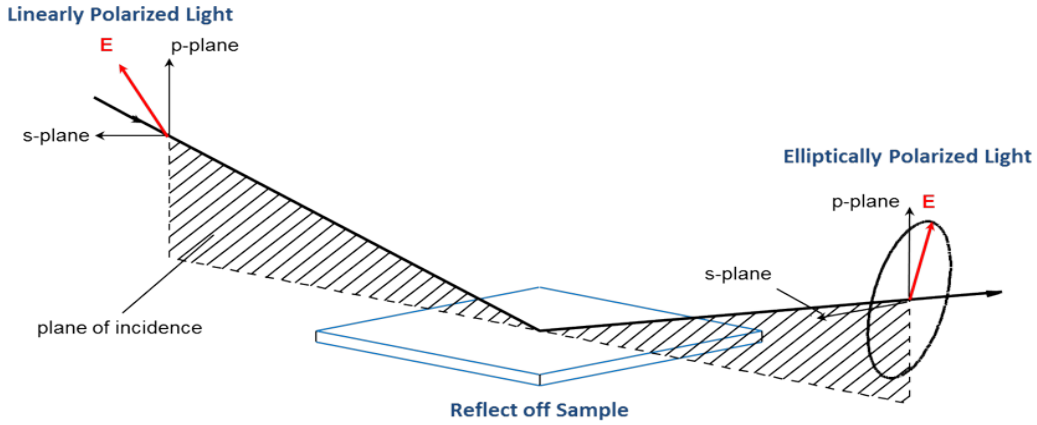

Figure 4: Schematic principle of ellipsometry [8].

A dedicated electrochemical-ellipsometry cell allows both optical and electrochemical measurements [9]. In our setup this cell is integrated into a three–electrode arrangement driven by a BioLogic SP–150e potentiostat and observed by a Woollam M–2000 ellipsometer.

Figure 5: Ellipsometry EC angle-of-incidence 70◦ measurement cell used in this work.

The starting model in CompleteEASE represents the evaporated gold sample as the substrate. The AuNP layer is taken as a Bruggeman effective medium of gold and electrolyte. The thickness and effective-medium (EMA) composition of this layer are determined by fitting the measured (Ψ, Δ) spectra. After protein immobilization, two additional sublayers are introduced to represent the filamentous protein coverage: a Cauchy component with $n \approx 1.45$ for the protein, and underlying Sellmeier–type water indices adjusted to match HEPES buffer.

Results

Optical modelling example

Layer Commands: Add Delete Save
Include Surface Roughness = OFF
Layer # 1 = EMA Thickness # 1 = 23.87 nm (fit)
# of Constituents = 2
+ Material 1 = H2O (Sellmeier)
Material 2 = Au_nk1
EMA % (Mat 2) = 10.2 (fit)
depolarization = 0.333 Analysis Mode = Bruggeman
Substrate = Au_nk1
Angle Offset = 0.00
+ MODEL Options
+ FIT Options
+ OTHER Options
Configure Options
Turn Off All Fit Parameters

Figure 6: Single–layer optical model in CompleteEASE. This model was obtained for a sample deposited at −350 mV, 2 mM concentration and 1 min deposition time, in contrast to earlier deposition conditions.

Fig. 6 illustrates how the fitted thickness and effective optical constants of the AuNP film are extracted from the measured (Ψ, Δ) spectra. In a next step the model is extended by additional dielectric layers to describe protein adsorption.

Voltammogram and morphology of a CV–grown film

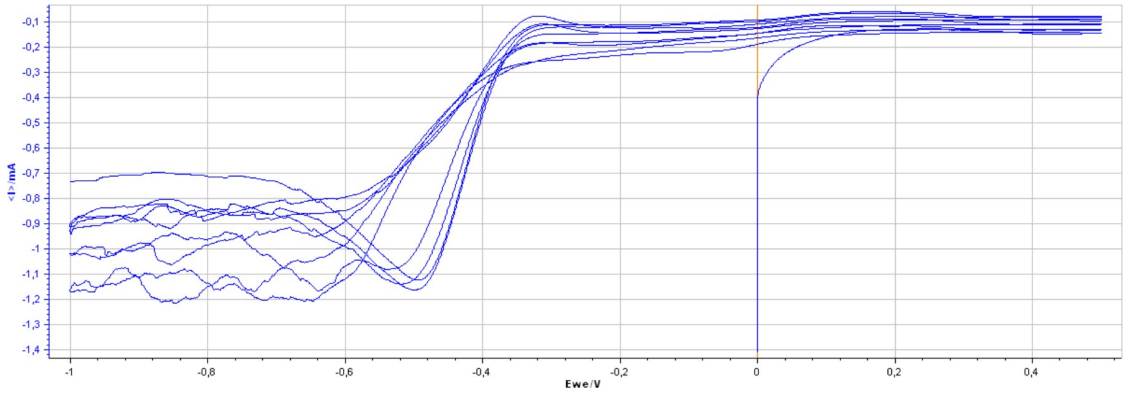

Figure 7: Cyclic voltammogram for a sample prepared by 5 CV cycles between −1.0 and +0.5 V at 2 mV/s in a 2 mM $HAuCl_4$ solution. The same sample was later imaged by SEM in Fig. 8.

A broad redox feature under the voltammogram is associated with the charge passed during protein immobilization. Comparing the integrated charge of subsequent cycles shows that the second cycle carries less charge than the first, indicating that available binding sites are progressively filled and start to run out. On the left (strongly cathodic) side of Fig. 7 the trace appears “hairy”. In this potential range the system is so cathodic that hydrogen evolution and other side reactions start: gas bubbles nucleate and detach from the surface, the local surface state changes and small convection eddies form. All these effects continuously change the effective active area and the diffusion layer thickness, so the recorded current flickers and the curve looks noisy. On the anodic side no significant gas evolution or rough surface transformation occurs; only a small, fairly steady background current flows, therefore the line is smooth.

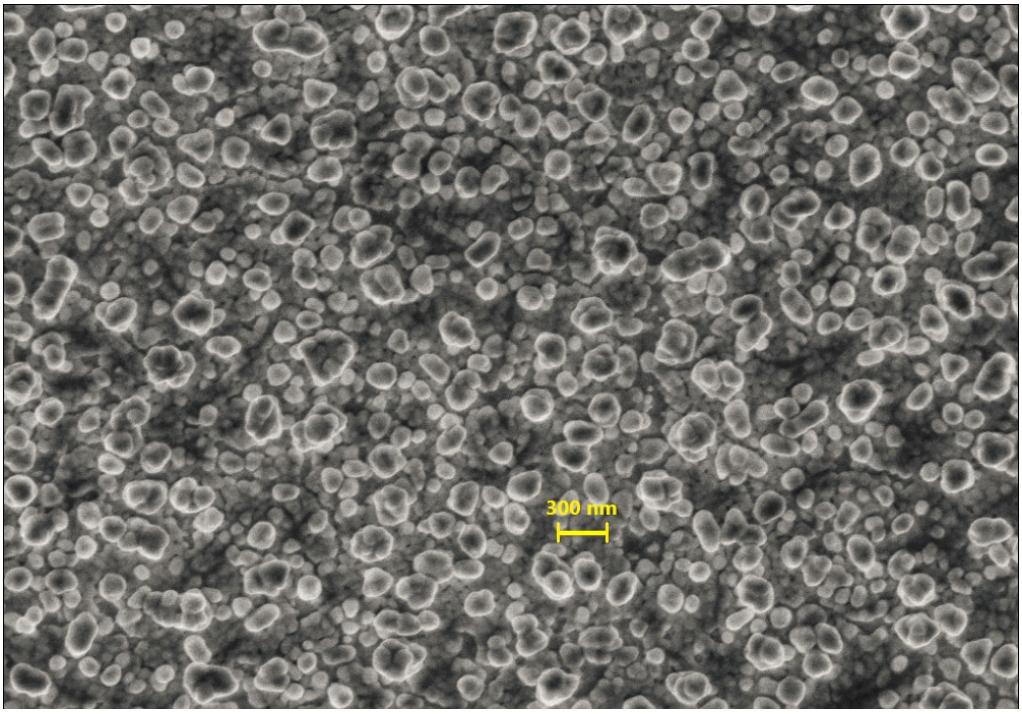

Figure 8: SEM image of the protein–covered AuNP surface for the same sample as in Fig. 7, recorded at 50,000× magnification. The film was formed by 5 CV cycles between −1.0 and +0.5 V at 2 mV/s in a 2 mM HAuCl4 solution.

The SEM image confirms a continuous AuNP coverage with additional filament–like protein structures visible on top of the nanostructured gold.

Discussion

The CA and CV programs together determine AuNP morphology (particle size, coverage, roughness) and, consequently, the density of available binding sites for protein immobilization. The electrochemical ellipsometry setup provides in situ feedback on film growth and protein adsorption, while SEM offers an ex situ morphological cross–check, reproducing a multi–aspect evaluation.

The noisy behaviour on the cathodic side of Fig. 7 illustrates typical side effects that can happen: hydrogen evolution and other reduction processes, bubble formation and detachment, local surface activation/passivation and forced convection. These phenomena modulate the effective electrode area and the diffusion layer in time.

Conclusions

We have presented a workflow to form AuNP–deposited gold films on silicon, to immobilize bioengineered protein filaments, and to monitor layer formation in situ by spectroscopic ellipsometry and ex situ by SEM, alongside CV/CA characterisation. We discuss the electrochemical background of AuNP deposition and protein binding, the ellipsometric modelling strategy, and the joint evaluation of voltammograms and SEM images. The approach supports the development of portable heavy–metal sensors for Ni(II) detection

in drinking water, providing quantitative electronic results instead of subjective colour comparison.

Acknowledgements. The project supported by the Doctoral Excellence Fellowship Programme (DCEP) is funded by the National Research Development and Innovation Fund of the Ministry of Culture and Innovation and the Budapest University of Technology and Economics.

References

[1] Braga, M. S., Jaimes, R. F. V. V., Borysow, W., Gomes, O. F., Salcedo, W. J.: Portable Multispectral Colorimeter for Metallic Ion Detection and Classification, *Sensors* 17 (2017) 1730.

[2] Sensafe: Econo-Quick Rapid Arsenic Test Kit for Water Analysis, product information, available at https: //sensafe.com/arsenic-kits.

[3] Labadi, Z. *et al.*: Sensing Layer for Ni Detection in Water Created by Immobilization of Bioengineered Flagellar Nanotubes on Gold Surfaces, *ACS Biomaterials Science and Engineering* 6 (2020) 3811–3820.

[4] Kurunczi, S. *et al.*: In situ ellipsometric study of surface immobilization of flagellar filaments, *Applied Surface Science* 257 (2010) 319–324.

[5] Kissinger, P. T., Heineman, W. R.: Cyclic Voltammetry, *J. Chem. Educ.* 60 (1983) 702–706.

[6] Elgrishi, N. *et al.*: A Practical Beginner's Guide to Cyclic Voltammetry, *J. Chem. Educ.* 95 (2018) 197–206.

[7] Fujiwara, H.: *Spectroscopic Ellipsometry: Principles and Applications*, Wiley, 2007.

[8] J.A. Woollam Co.: *What is Ellipsometry*? Ellipsometry FAQ, available at https://www.jawoollam. com/resources/ellipsometry-faq.

[9] Redox.Me: Ellipsometry EC Angle of Incidence 70° Cell, product information, https://redox.me/ products/ellipsometry-ec-angle-of-incidence-70-deg

Structural characterisation of the DC-sputtered $Al_{1-x}Cu_x$ thin layer system

Dániel Olasz[1,2], Noémi Szász[1], Tamás Kolonits[1], György Radnóczi[1], Nguyen Quang Chinh[2], György Sáfrán[1]

[1] Institute for Technical Physics and Materials Science, HUN-REN Centre for Energy Research, Konkoly-Thege 29-33, Budapest 1121, Hungary

[2] Depratment of Materials Physics, Eötvös Loránd University, Pázmány Péter sétány 1/A, Budapest 1117

The Al–Cu binary thin layer system was prepared over the entire composition range (0–100 at% Cu) using micro-combinatorial variable-power DC magnetron co-sputtering of the constituents [1]. Fifteen individual $Al_{100-x}Cu_x$ layers were deposited side-by-side on a single Si substrate under identical vacuum conditions, ensuring that composition was the only, systematically varied, parameter.

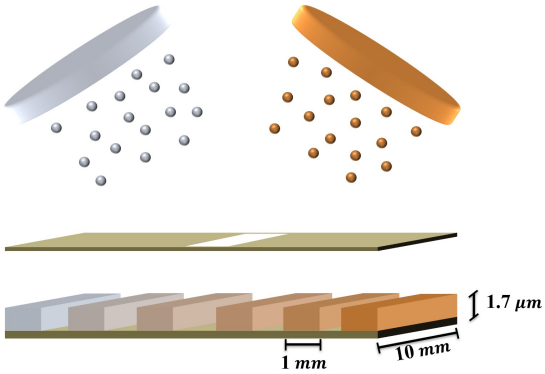

Fig. 1: Schematic arrangement of deposition of Al-Cu layers with varying composition through a positionable slit.

Cross-sectional TEM (XTEM), selected area electron diffraction (SAED), high-angle annular dark-field (HAADF) imaging, and STEM-EDS elemental mapping were applied to determine composition, phases and morphology of the layers.

The pure Al thin film exhibits a columnar structure of vertically elongated grains with typical widths of ~350 nm. SAED confirm the exclusive presence of the fcc α-Al phase. Even small Cu additions have a dramatic effect on the microstructure of the layer. At Cu contents as low as 4 at%, the grain width of the α-Al phase decreases to ~150 nm, accompanied by the appearance of the Θ-Al_2Cu intermetallic phase in the form of small (~60 nm) precipitates. HAADF imaging and elemental maps reveal a relatively uniform spatial distribution of these Θ-phase particles within the Al matrix. With increasing Cu concentration (8–17 at%), the volume fraction of the Θ phase increases, while the α-Al grain size continues to decrease. At 30 at% Cu, the Θ-Al_2Cu phase becomes dominant, and α-Al is mainly confined to grain boundary regions.

In the near-equiatomic composition range, the microstructure differs from that predicted by the eq. phase diagram. XTEM and SAED analyses reveal the formation of the non-equilibrium γ-Al_4Cu_9 intermetallic phase, either coexisting with Θ-Al_2Cu (at ~41 at% Cu) or appearing as the sole crystalline phase (52–61 at% Cu).

These films exhibit a highly refined columnar structure with an average column width of ~40 nm. The formation of the γ-Al_4Cu_9 phase is attributed to the high deposition rate and low substrate temperature, promoting non-eq. phase formation.

Cu-rich layers primarily consist of the fcc α-Cu solid solution, with the γ-Al_4Cu_9 by-phase present only at 70 at% Cu. At higher Cu concentrations (≥77 at%), α-Cu becomes the exclusive crystalline phase. High density of stacking faults is observed, increasing with Al content, consistent with the low stacking fault energy of Cu.

This work on characterizing Al–Cu thin film system demonstrates that the combination of micro-combinatorial synthesis and XTEM enables comprehensive investigation of phase formation and microstructure evolution in entire binary thin film systems.

Acknowledgement: The authors acknowledge the support of the National Research, Development and Innovation Fund of Hungary under projects No. K143216 and NKFIH-ADVANCED-153100. The support provided by VEKOP-2.3.3–15–2016–00002 of the European Structural and Investment Funds is greatly acknowledged. The research of NQC, DO and GS was also supported by the Hungarian-Russian bilateral Research program (T É T) No. 2021–1.2.5-T É T-IPARI-RU-2021–00001.

References:

[1] D. Olasz, N. Szász, T. Kolonits, G. Radnóczi, N.Q. Chinh, G. Sáfrán; J. Alloys Compd. 2026, 1051, 186114. https://doi.org/10.1016/j.jallcom.2026.186114

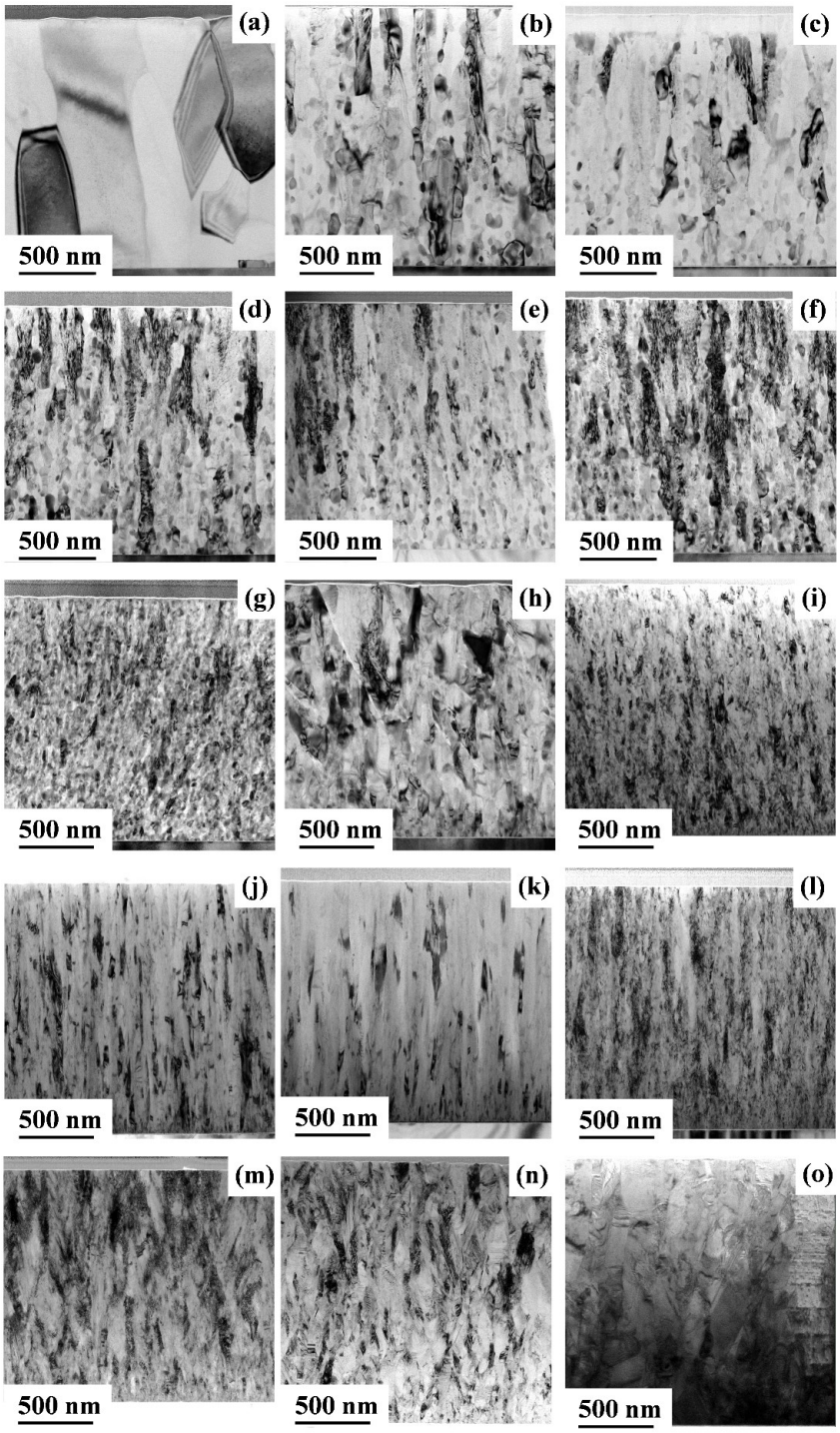

Figure 2: *XTEM micrographs of the layers a) Pure Al b) $Al_{96}Cu_4$ c) $Al_{95}Cu_5$ d) $Al_{94}Cu_6$ e) $Al_{92}Cu_8$ f) $Al_{91}Cu_9$ g) $Al_{83}Cu_{17}$ h) $Al_{70}Cu_{30}$ i) $Al_{59}Cu_{41}$ j) $Al_{48}Cu_{52}$ k) L11 $Al_{39}Cu_{61}$ l) L12 $Al_{30}Cu_{70}$ m) $Al_{23}Cu_{77}$ n) $Al_{16}Cu_{84}$ o) Pure Cu.*

A novel, photoassisted synthetic route to transform Cu_2O nanooctahedra to Cu_2S quantum-dot superstructures

OTKA FK142148; TKP2021-NKTA-05

*D. Kovács, G. Z. Radnóczi, Zs. E. Horváth, K. Frey, A. Sulyok, Z. Fogarassy, J. S. Pap, A. Deák, D. Zámbó**

Institute for Technical Physics and Materials Science, HUN-REN Centre for Energy Research, Konkoly-Thege 29-33, Budapest 1121, Hungary

The family of copper sulfides includes numerous materials, which are relevant in minerology as well as in nanoscience and possess various stoichiometries (hence, they can be denoted as $Cu_{2-x}S$, where the $0<x<1$). For well-defined nanocrystals or nanoparticle-based materials, the structure, composition and stoichiometry have a profound impact on the optical and electrochemical properties. The main challenge in synthesizing copper chalcogenides is closely connected to the ability of natural oxidation and sulfidation of chalcophile metals such as Cu or Ag. This technically means that copper sulfides and oxides tend to oxidize and sulfidize at ambient conditions, respectively.

In the recent years we have developed a reliable strategy for the synthesis of Cu_2O nanooctahedra showing excellent morphological stability, tunable optical and enhanced catalytic activity. However, even in optimized storage conditions (dark, 4°C, ethanol as solvent), the particles' composition and morphology slightly changed after 8 months of storage. We have shown that the particles undergo partial natural sulfidation which phenomenon can be linked to the presence of thiolated molecules and inorganic sulfur compounds in the atmosphere. This natural process motivated us to develop a novel strategy of the transformation of Cu_2O nanooctahedra to copper sulfide particles by using a small-chain thiolated alcohol (*β-mercaptoethanol, BME*) to initiate the oxide-sulfide transition wet-chemically. [1] The schematics in Figure 1 shows the steps of the synthesis.

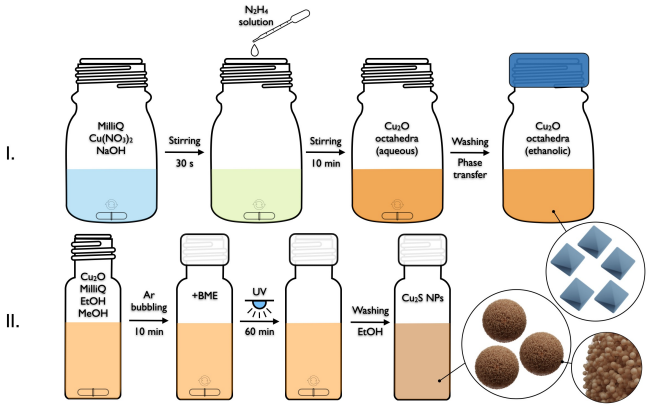

***Figure 1**. Schematics on the synthesis of Cu_2O nanooctahedra and their photoassisted chemical transformation to Cu_2S quantum-dot superstructures. [1]*

The presence of mercaptoethanol itself does not generate well-defined copper sulfide species due to the oxidation and sulfidation occurring simultaneously at ambient conditions. This results in partially sulfidize particles and overoxidized (CuO) fibers in the solution. This oxidation pathway can be successfully eliminated by applying inert atmosphere (Ar) and UV-light illumination enabling the reliable synthesis of colloidally stable, spherical copper sulfide particles. The optical properties change

stepwise upon increasing the amount of added BME showing a shifting peak position from ca. 550 nm to 400 nm and a broadening (Figure 2a). Interestingly, the TEM investigations reveal the presence of small (4-5 nm) quantum dots building up the larger copper sulfide particles. Moreover, the dots are separated by an amorphous organic thin layer. Elemental mapping confirmed that the ca. 250 nm in diameter spheres consist of Cu and S, and the low amount of O is present (Figure 2b). However, this oxygen content cannot be further suppressed, which implies the existence of a stable copper sulfide phase and another oxygen-containing species.

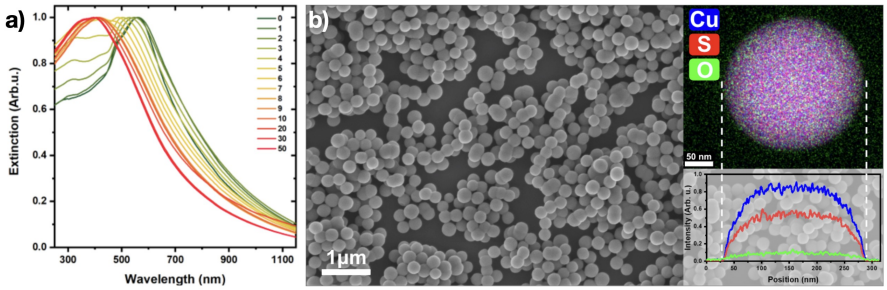

Figure 2. *Evolution of the extinction spectrum upon increasing the concentration of BME (a). SEM image and TEM elemental map of the Cu_2S particles (b). [1]*

Performing advanced TEM sample preparation method and SAED, the precise stoichiometry and phase of the nanospheres could be identified (Figure 3a-c). The sulfidized particles are superstructures consisting of small Cu_2S quantum dots, which are separated by a thin layer of organic thiol. Furthermore, these spherical particles can be decorated with small Au nanograins to achieve a semiconductor-metal multicomponent nanosystem, where the photogenerated carriers can be spatially separated. Macroscopic electrodes from the Cu_2S and Cu_2S/Au particles can be prepared on a conductive substrate, thus, the electrochemical properties of the model systems were also investigated. Open circuit potentiometry (Figure 3d) revealed that all synthesized nanoparticle electrodes show p-type nature and the presence of Au suggests an enhanced charge carrier separation. Under chopped light illumination, the electrodes generate cathodic current which reaches the maximum value of 50 μAcm^{-2} for the Cu_2S@Au platform (Figure 3e). After negative polarization, the particles at the surface of the ITO remain morphologically stable (Figure 3f) which suggest their potential use in (photo)electrochemical processes. [1]

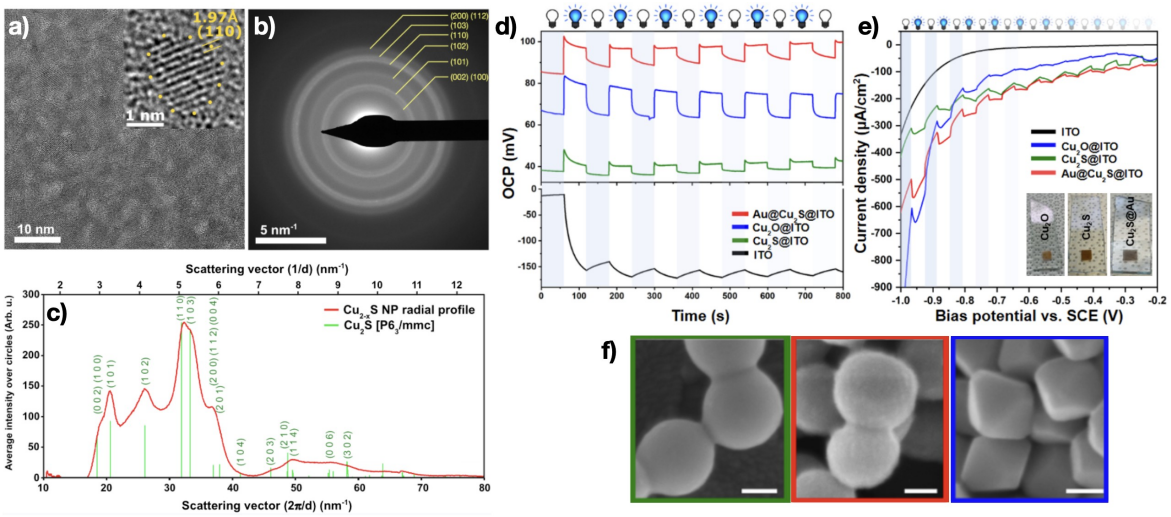

Figure 3. *Phase identification (a-e) and electrochemical investigations (d-f) on the synthesized nanoparticles. [1]*

Regarding the formation mechanism of the Cu_2S quantum-dot superstructures the following pathway can be proposed (Figure 4): reactive sulfur species (RSS) are formed from the organic thiol upon high-energy UV illumination facilitating first the homolytic cleavage of the S-H bond or the disulfide (S-S) bond. These (most probably thiyl) radicals can interact with the surface Cu centers of the copper oxide nanoparticles initiating a gradual anion (from O to S) in the sublattice. Simultaneously, UV light generates charge carriers in the Cu_2O itself, from which the electrons are able to reduce the surface-bound organocopper species to provide sulfur for the ion exchange reaction. This work sheds light on the complex formation mechanism, the optimal conditions and the optical, structural and electrochemical properties of novel Cu_2S superstructures prepared from Cu_2O sacrificial template. [1]

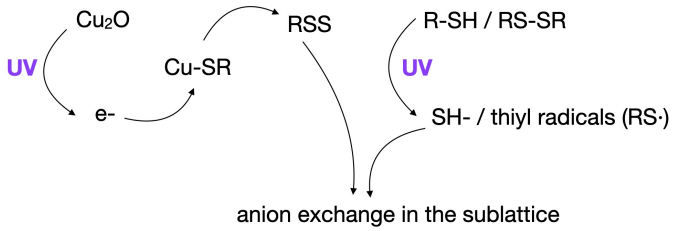

Figure 4. *Proposed mechanism of the Cu_2O-Cu_2S photoassisted transformation process.*

Acknowledgement: D.K. acknowledges the support of Pro Progressio and the József Varga Foundation. Project no. TKP2021-NKTA-05 has been implemented with the support provided by the Ministry of Innovation and Technology of Hungary from the National Research, Development, and Innovation Fund (NRDI), financed under the TKP2021 funding scheme. The work was financially supported by the NRDI Fund of Hungary under the grant OTKA FK 142148.

References:

[1] Kovács, D.; Radnóczi, G. Z.; Horváth, Z. E.; Frey, K.; Sulyok, A.; Fogarassy, Z.; Pap, J. S.; Deák, A.; Zámbó, D. Photoassisted Chemical Transformation of Cu_2 O Nanooctahedra into Cu_2 S Quantum-Dot Superstructures: Structural and Photoelectrochemical Properties. *ACS Mater. Au* **2025**, 5, 6, 1018–1028 https://doi.org/10.1021/acsmaterialsau.5c00106.

The work has been selected as the „Paper of the month" by the Section of Chemical Sciences of the Hungarian Academy of Sciences in September, 2025: https://mta.hu/vii-osztaly-a-honap-publikacioja/2025-szeptemberi-kiemelt-publikaciok-114720

Spatial modulation of Cu_2O shell growth on gold nanoprisms.

Ziyoda Ganieva[1,2], Dávid Kovács[1], Zoltán Osváth[1], Dániel Zámbó[1],

and András Deák[1,*]

[1]HUN-REN Centre for Energy Research, Institute of Technical Physics and Materials Science, 1121 Budapest, Konkoly-Thege Miklós út 29–33., Hungary

[2]Institute of Chemistry University of Pécs Pécs H-7624, Hungary

andras.deak@ek.hun-ren.hu

Abstract. Structural control in metal/semiconductor multicomponent nanoparticles enables advanced functional properties by tailoring optoelectronic processes and the accessibility of individual components. This study investigates how surface-adsorbed molecules (5-amino-2-mercaptobenzimidazole, AMBI) influence the wet-chemical deposition of cuprous oxide (Cu_2O) shells on gold nanoprisms. Although gold and Cu_2O are generally highly compatible, the presence of AMBI strongly alters shell growth. Time-resolved optical and structural analyses reveal that AMBI significantly amplifies the intrinsic Volmer–Weber growth behavior of Cu_2O. Single-particle measurements attribute this effect to inhomogeneous, multi-patch surface coverage. Under optimized conditions, the nanoprism tips are effectively protected, remaining free of Cu_2O overgrowth.

Keywords: gold nanoprism, patchy particle, Cu_2O

Introduction

Environmentally friendly and earth abundant metal oxide semiconductors are intensively studied for optoelectronic and catalytic applications, but they suffer from low charge carrier mobilities, that represents a major obstacle for their large scale use. Nanoscale metal/metal-oxide nanoparticles might help in this regard, as at this scale recombination processes might be suppressed and a more efficient separation of the charge carriers generated in the semiconductor domain could be achieved.[1] Another advantage in such hybrid systems might come from the possibility to harvest hot carriers from the metal. Theoretically, the hot carriers generated in the plasmonic metal nanoparticles have to overcome only the Schottky barrier formed at the metal/oxide semiconductor interface, hence charge injection into the semiconductor and contribute to the efficiency of optoelectronic processes at the semiconductor. In this regard, partial core/shell structures are especially appealing, as they allow the simultaneous access both the metal and semiconductor domains. Cu_2O is a p-type semiconductor with its optical band-gap located in the visible wavelength range and has an excellent combability with gold, allowing the wet-chemical growth of a Cu_2O shell around gold nanoprisms. [2]

Results and discussion

In this work we used the controlled spatial modulation of the gold nanoprisms' surface energy to partially prevent Cu_2O deposition on gold nanoprisms. [3] The approach relies on the inhomogeneous accumulation of a thiol molecule (5-amino-2-mercaptobenzimidazole - AMBI) on the prisms' surface during a surface modification reaction prior to Cu_2O deposition. AMBI is known to effectively block the deposition of Cu_2O on gold nanoparticles, provided it is present at a sufficient high packing density at the interface. Nevertheless, achieving a proper molecule packing on the particle surface depends heavily on the concentration of the AMBI molecules and the applied temperature during surface modification. At higher temperature it can be anticipated that the higher mobility at the interface leads to higher packing density. This is demonstrated by performing the Cu_2O shell deposition at different temperatures, leading to the formation of a thin shape conform shell (Figure 1a). This indicates that despite the presence of AMBI molecules at the prism surface, a neat coating is formed. Hence, the surface density of molecules is too low for the effective modulation of the shell morphology. Nevertheless, the surface adsorbed molecules slow down the Cu_2O shell growth, as inferred from time evolution of the prisms' dipolar plasmon peak position shift which is clearly observed in the beginning phase (first 2 minutes) of the growth process (Figure 1b). At the end of the growth process, however, the same redshift as for the untreated sample is achieved, consistent with TEM image showing a complete Cu_2O shell around the prisms. When the same amount of AMBI molecule is used, but the temperature is increased to 60 °C during molecule adsorption, there a profound difference in the time evolution of the dipolar plasmon peak is observed. Not only get the redshift much slower (Figure 1a), its final value is also significantly smaller that for the untreated, or room temperature sample (Figure 1c). This indicates already that during the surface modification carried out at 60 °C, higher density molecular patches are formed, that can partially block the deposition of Cu_2O on the particle surface.

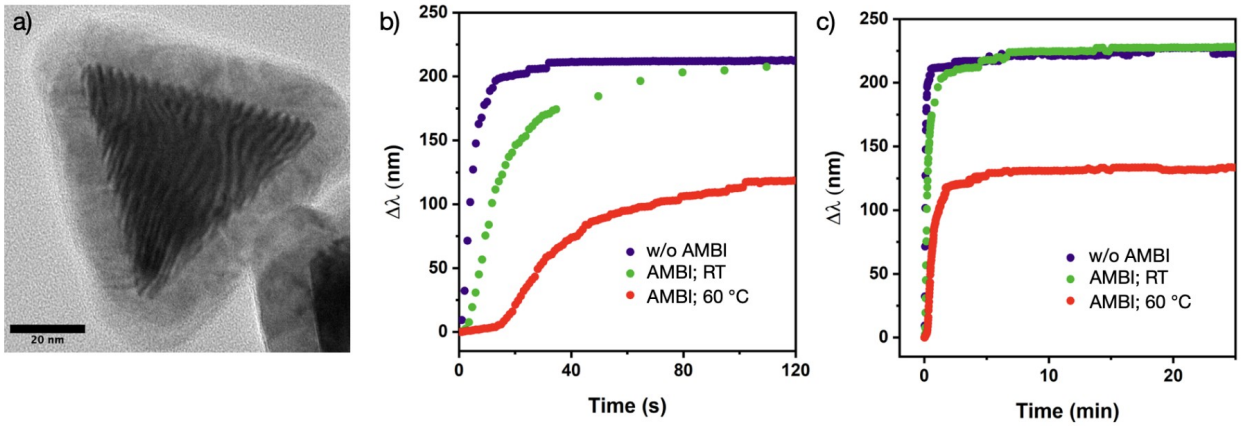

Figure 1. TEM image of a nanoprism treated with AMBI (1 µM AMBI, c(Au0)=315 µM) at room temperature before Cu_2O deposition (a). The prisms' dipolar plasmon resonance peak shift as a function of time during the shell growth during the first 2 minutes (b) and the total course of the shell growth procedure (c). [3]

To investigate the underlying cause for the observed spectral differences during Cu_2O shell growth, scanning probe microscopy measurements on individual nanoparticles. Under appropriate conditions in terms of reaction temperature and AMBI concentration, submonolayer coverage of the prisms can be achieved, showing the presence of some high density molecular patches (Figure 2). Already at concentrations that show a patchy AMBI adsorption at the nanoprisms' flat faces (Figure 2b), almost complete coverage of the side and tip regions can be anticipated due to the higher energy binding sites in these regions, which can be exploited the reduce the Cu_2O deposition in these particle regions during the wet-chemical growth of the shell.

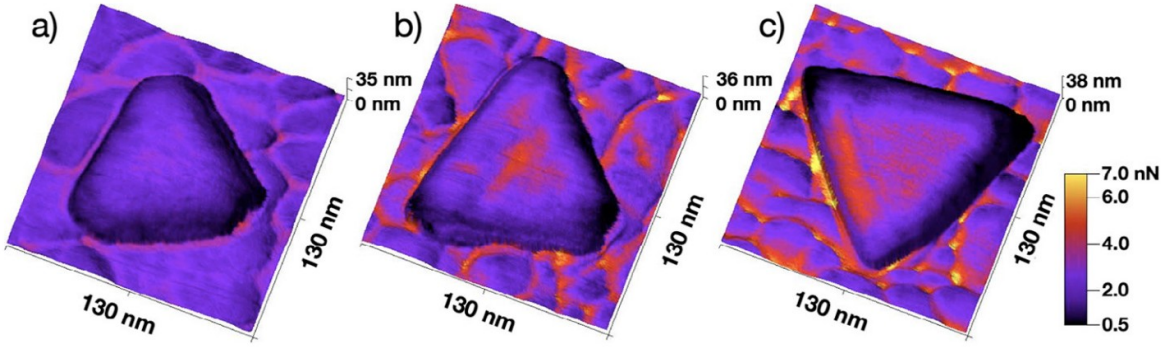

Figure 2. Scanning probe microscopy derived topography of the indium tin oxide supported nanoprisms overlain with the adhesion force maps: no AMBI treatment a) and surface modification at 1 µm b), and 190.5 µm AMBI c).[3]

This was confirmed by investigating the evolution of the Cu_2O shell structure over the reaction time, quenching the process at different time instances and investigating the particle morphology ex-situ by transmission electron microscopy (Figure 3). If AMBI is absent, Cu_2O forms a neat shell around the gold nanoprisms in a shape conform manner (top row). When the gold nanoprisms are pretreated with AMBI under optimised conditions, however, strong structural inhomogeneity of the shell develops. The number of nucleation sites is strongly reduced, which is especially clear in the early phase of the shell growth. It has to be stressed that the few Cu_2O domains on the prism surface in the presence of AMBI in the beginning phase (15 s) agreed well with the scanning probe microscopy derived adhesion map pattern. Nevertheless the observed Moiré pattern for these few dots indicates that the excellent compatibility between the gold and Cu_2O is preserved at the nucleation sites. At later growth stages the initial Cu_2O domains grow larger and fuse together. It seems, however, that

the combination of AMBI coverage and the surface curvature at the prism tips effectively prevents the growing and fusing Cu_2O domains to engulf the prism tips, leaving then exposed even after the competition of the growth process. The prepared structure ensures the simultaneous access of both the metal and semiconductor domains, and hence can be of interest for optoelectronic and catalytic use. Additionally, the high optical near field at the prism tips that develop upon exciting localised plasmons at the prisms can also be utilised.

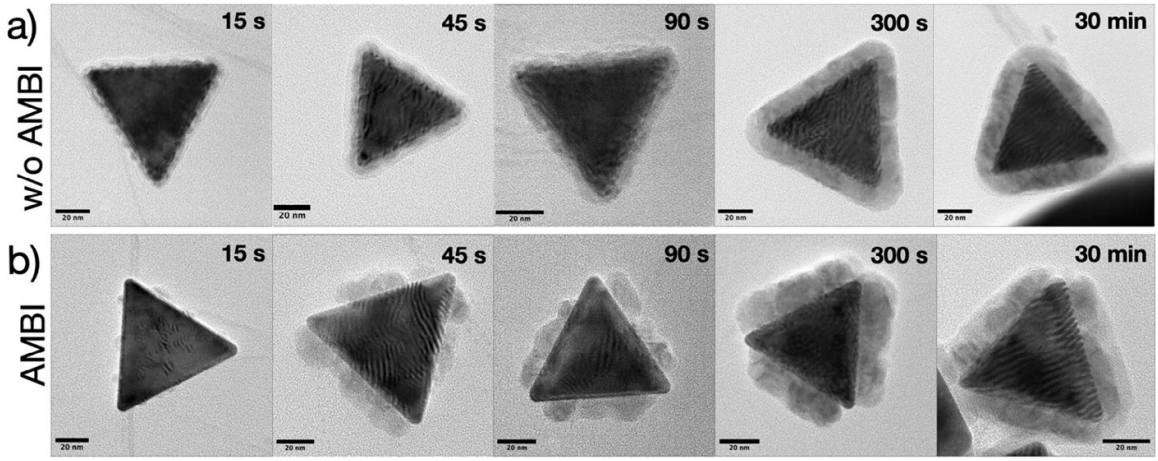

Figure 3. TEM images of the Cu2O/Au nanoparticles prepared without (upper row) and in the presence of AMBI (lower row).[3]

Conclusions

High-density molecular patches on gold nanoprism surfaces enable spatial control of Cu_2O deposition by locally modifying surface energy at the nanoscale. Sub-monolayer molecular coverage disrupts the otherwise shape-conformal Cu_2O shell and effectively protects the prism tips from overgrowth (Figure 4). Time-resolved spectroscopic and electron microscopy studies show that Cu_2O deposition on surface-modified nanoprisms is strongly suppressed during the early growth stages, initiating instead at well-separated nucleation sites that persist throughout shell formation. The prism tips remain uncoated, likely due to higher molecular coverage caused by curvature and initial ligand density effects. The patchy molecular coating is further confirmed by scanning probe microscopy on individual nanoprisms. Such site-selectively overcoated metal/semiconductor nanoparticles are promising for optoelectronic applications, as they combine intimate phase contact with access to high-intensity plasmonic near fields.

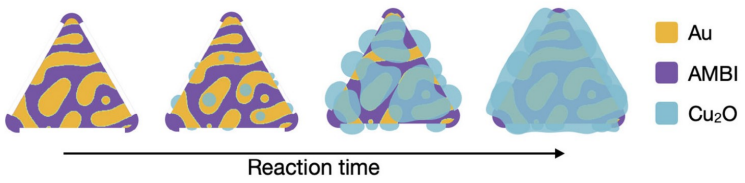

Figure 4. Possible shell growth mechanism based on the transmission electron and scanning probe microscopy measurements. [3]

Acknowledgements. D.K. acknowledges the support of Pro Progressio and the József Varga Foundation. The work was financially supported by the NRDI Fund of Hungary under the grant OTKA FK 142148. Project no. TKP2021-NKTA-05 has been implemented with the support provided by the Ministry of Innovation and Technology of Hungary from the National Research, Development and Innovation Fund (NRDI), financed under the TKP2021 funding scheme. Z.O. acknowledges the financial support from the National Research, Development and Innovation Office (NKFIH) in Hungary, through the Grant No. K-134258. Funding: National Research, Development and Innovation Fund (NRDI) FK-142148, TKP2021-NKTA-05, K-134258.

References

[1] Kovács, D.; Deák, A.; Radnóczi, G. Z.; Horváth, Z. E.; Sulyok, A.; Schiller, R.; Czömpöly, O.; Zámbó, D. Position of Gold Dictates the Photophysical and Photocatalytic Properties of Cu2O in Cu2O/Au Multicomponent Nanoparticles. J. Mater. Chem. C 2023, 11 (26), 8796–8807.

[2] Zámbó, D.; Kovács, D.; Deák, A. Optical and Structural Properties of Cuprous Oxide Shell Coated Gold Nanoprisms. Part & Part Syst Charact 2024, 2400082.

[3] Ganieva, Z.; Kovács, D.; Osváth, Z.; Zámbó, D.; Deák, A. Region-Selective Growth of Cu2 O Shell on Gold Nanoprisms. Adv Materials Inter 2025, 12 (16), e00512.

A new method to evaluate multi-color ellipsometric mapping on big area samples

*Sándor Kálvin[1], Berhane Nugusse Zereay[1,2,4], György Juhász[1], Csaba Major[1], Péter Petrik[1,3], Zoltán György Horváth[1] and Miklós Fried[1,2] **

[1]Institute of Technical Physics and Materials Science, Centre for Energy Research, Konkoly-Thege Rd. 29-33, Budapest 1121, Hungary
[2]Institute of Microelectronics and Technology, Obuda University, Tavaszmezo Str. 17, Budapest 1084, Hungary
[3]Department of Electrical Engineering, Institute of Physics, Faculty of Science and Technology, University of Debrecen, 4032 Debrecen, Hungary
[4]Mai Nefhi College of Science, Asmara, Maekel, Eritrea
* Correspondence: fried.miklos@ek-cer.hu

Abstract

Ellipsometric mapping measurements and Bayesian evaluation were performed with a non–collimated, imaging ellipsometer using an LCD monitor as a light source. In such a configuration, the polarization state of the illumination and the local angle of incidence vary spatially and spectrally, rendering conventional spectroscopic ellipsometry inversion methods hardly applicable. To address these limitations, a multilayer optical forward model is augmented with instrument–specific correction parameters describing the polarization state of the monitor and the angle–of–incidence map. These parameters are determined through a Bayesian calibration procedure using well–characterized Si-SiO_2 reference wafers. The resulting posterior distribution is explored by global optimization based on simulated annealing, yielding a maximum a posteriori estimate, followed by marginalization to quantify uncertainties and parameter correlations.

The calibrated correction parameters are subsequently incorporated as informative priors in the Bayesian analysis of unknown samples, including polycrystalline–silicon layers deposited on Si-SiO_2 substrates and additional Si-SiO_2 wafers outside the calibration set. The approach allows consistent propagation of calibration uncertainties into the inferred layer parameters and provides credible intervals and correlation information that cannot be obtained from conventional least–squares methods.

The results demonstrate that, despite the broadband nature of the RGB measurement and the limited number of analyzer orientations, reliable layer thicknesses can be obtained with quantified uncertainties for a wide range of technologically relevant samples. The proposed Bayesian framework enables a transparent interpretation of the measurement accuracy and limitations, and provides a robust basis for large–area ellipsometric mapping of multilayer structures.

Keywords: optical mapping, multi-color ellipsometry, pinhole camera, Bayesian inference, simulated annealing

1. Introduction

Non–destructive characterization techniques play a fundamental role in thin–film technology. Spectroscopic ellipsometry (SE) is one of the most widely used methods, providing information on layer thicknesses and optical constants by analyzing the change in polarization state of a reflected or transmitted beam. The measured quantities are the real and imaginary part of the complex reflectance ratio (ρ), the amplitude ratio $\tan\psi$ and the phase difference Δ between the parallel (p) and normal (s) polarization components. [1-4]

For simple sample structures SE data can be inverted analytically, but for general multilayer systems a numerical model is required. The model predicts $\psi(\lambda)$ and $\Delta(\lambda)$ spectra, and the parameters of the layer stack are obtained by minimizing the discrepancy between measured and simulated spectra. Conventional SE works extremely well when the instrument provides many wavelength points, a well–defined angle of incidence, and stable optics; under such conditions the merit function is sharply peaked and yields a unique optimum.

However, standard numerical optimization tends to become trapped in local minima when the available spectral information is limited or when the forward model contains uncertainties. Global–search techniques such as simulated annealing (SA) can mitigate this problem by exploring the parameter space more broadly.

Simulated annealing is a global optimization algorithm designed to find the global minimum or maximum of any given function. [5-7] It is completely general in that it entails in principle no restrictions on the function

to be minimized. In the case of ellipsometry data analysis, no assumptions need to be made about the sample's physical properties. However this technique supply only the most probably parameters without any information about the uncertainties of the layer parameters.

The optical–mapping ellipsometer used in this work differs fundamentally from classical spectroscopic ellipsometry [8]. Instead of recording hundreds of narrowband wavelength points, our system acquires only three broad spectral channels (R, G, B) at four analyzer orientations. Each measured intensity is an integral over a wide wavelength band, and the resulting inverse problem becomes inherently underdetermined. As a consequence, the conventional SE inversion chain $I \rightarrow S_1, S_2 \rightarrow \psi, \Delta \rightarrow \rho \rightarrow \sum$ (Intensities, Stokes-parameters, amplitude ratio, phase shift, complex reflectance, physical parameters of sample) cannot be applied, because wavelength–resolved Stokes parameters can be hardly determined for our instrument. Multiple parameter combinations can reproduce the same RGB intensities, giving rise to ambiguity, strong correlations, and non–unique solutions.

The inverse problem arising from RGB optical–mapping ellipsometry is therefore inherently Bayesian in nature. The limited amount of spectral information implies that the measured data alone are insufficient to uniquely determine all unknown parameters. Bayesian Probability Theory (BPT) [9-12] provides a natural and consistent framework to address this situation by treating all unknown quantities probabilistically and by explicitly incorporating prior physical knowledge, such as realistic parameter ranges, smoothness constraints, and independent calibration information. Within this framework, the likelihood function describes the statistical properties of the measured intensities, while the posterior distribution quantifies parameter correlations, degeneracies, and uncertainty intervals in a statistically meaningful way.

An additional challenge of the present problem is that the data evaluation itself is inherently multi–stage. The calibration of the optical–mapping ellipsometer is not a simple preprocessing step, but a probabilistic inference problem in its own right. Instrument-specific correction parameters and angle-of-incidence map must first be inferred from dedicated calibration samples, together with their associated uncertainties. These inferred calibration parameters and uncertainties are then used as prior information in the subsequent analysis of unknown samples, such as polycrystalline–silicon layers. This sequential propagation of uncertainty — from calibration to sample analysis — cannot be handled consistently within conventional deterministic inversion schemes and constitutes a central motivation for the Bayesian approach adopted in this work.

In this work, Bayesian inference is not used as an optional refinement, but as the core methodological framework for calibration, evaluation, and uncertainty quantification in RGB optical–mapping ellipsometry. Within this Bayesian framework, the numerical task of determining the most probable parameter values corresponds to locating the maximum of the posterior distribution. Due to the complex and often multimodal structure of the resulting objective function, a simulated–annealing global–search algorithm is employed as a robust numerical optimizer to reduce the risk of convergence to local minima.

We provide a critical assessment of conventional spectroscopic–ellipsometry data processing in the context of broadband RGB measurements. Through controlled numerical experiments we show that applying the classical inversion scheme to RGB data leads to significant and systematic errors in the recovered layer parameters, and we identify the physical reasons why this approach fails. Building on this insight, we develop a complete Bayesian data–analysis framework that consistently accounts for statistical and systematic uncertainties and treats instrument–specific correction factors and unknown sample parameters within a single probabilistic model.

The methodology is validated through extensive numerical experiments on synthetic data sets, which quantify the achievable accuracy and reveal the intrinsic limitations arising from broadband spectral information and non–collimated illumination. Finally, we demonstrate the practical applicability of the method on real SiO_2-Si and polycrystalline– silicon samples, showing that the Bayesian framework enables the reliable extraction of spatially resolved layer parameters over large areas together with meaningful uncertainty estimates.

This integrated methodology forms the foundation of the calibration, evaluation, and uncertainty–quantification procedures presented in the remainder of this paper.

2. Materials and Methods

2.1 Experimental setup

We know two industrial systems which are capable of measuring big (square-meter size) samples: the Semilab FPT system [13] and the Woollam AccuMap [14] system. These devices use a traditional SE system (with ~100 kUSD price) in a large moving or scanning arrangement, measuring the samples point-by-point. The measurement time is several tens of minutes. In contrast, our system is capable of performing the measurement within seconds in a single shot. [8]

The non-collimated beam ellipsometer setup is shown in Fig. 1 and 2. The system uses an LED–LCD monitor as a polarized, RGB-colored light source (the built-in polarizer sheet is marked as (4) in Fig. 2), and a polarization-sensitive camera behind a pinhole (see number 7&8) together. The LCD monitor (Dell UltraSharp™ U2412M, GB-LED) is used in a 45-degree rotated position. (The angle-position is measured by a digital angle gauge with 0.1 deg precision, see the top of the monitor on Fig. 1.) In a straight-through position, we can detect the extinction of the polarization-sensitive camera better than 10^{-2}.

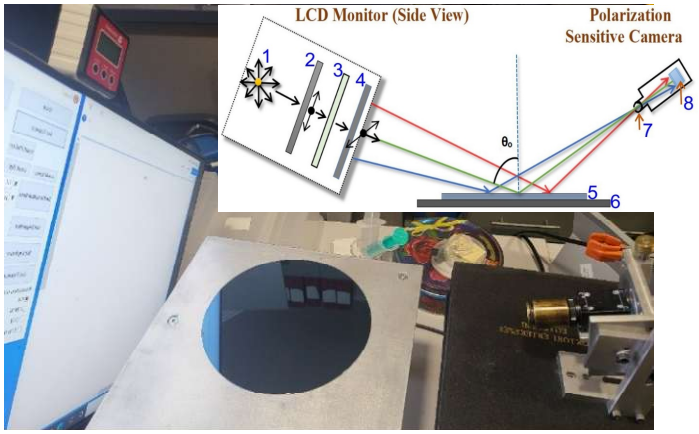

Figure 1. Experimental set-up: Polarization sensitive camera (8) with pinhole (7) (Right); Sample (5, oxide film on a 20 cm diameter Si-wafer) + Sample holder (6) (Middle); LCD monitor (1-4) rotated into 45° position with digital angle gauge (Left).

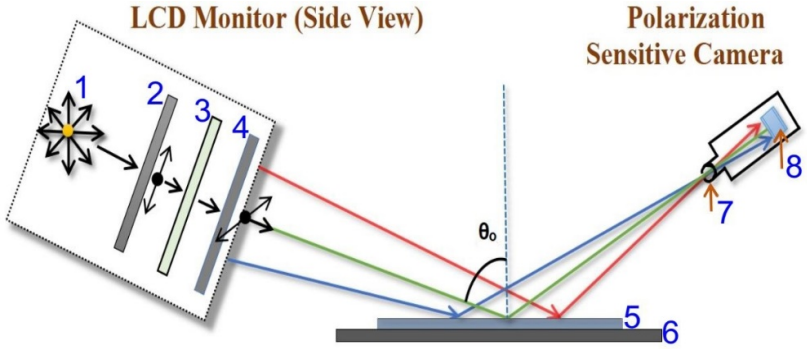

Figure 2. Schematics of the non-collimated beam ellipsometer (optical mapping tool made from cheap parts). (1) Light source. (2) Vertical polarizer. (3) Liquid crystal cell. (4) Horizontal polarizer. (5) Sample. (6) Sample holder. (7) Pinhole (sub-mm size). (8) Camera sensor.

Fig. 2 shows the LCD monitor as a light source (1-4), the sample holder (6), and the polarization-sensitive camera (8). The camera is the DYK 33UX250 USB 3.0 Polarsens model (The Imaging Source), equipped with a Sony CMOS Pregius Polarsens IMX250MZR sensor. This sensor includes a built-in, 4-direction wire-grid polarizer array. Fig. 3 shows its schematic design.

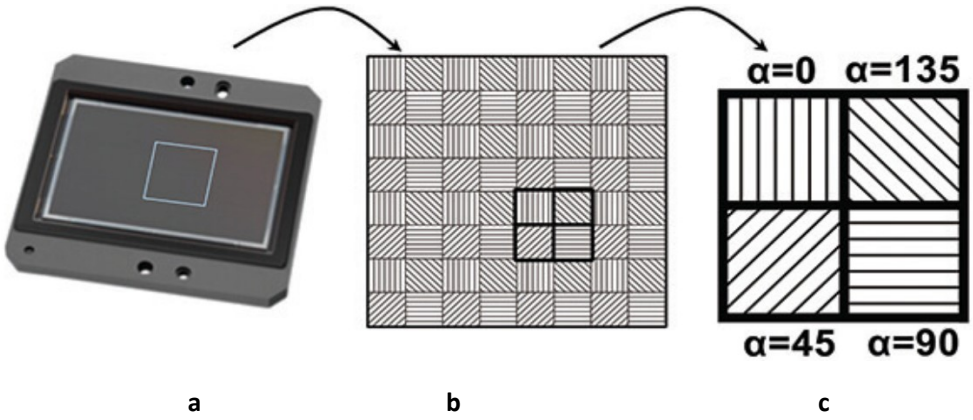

Figure 3. Schematic structure of a 2/3 inch Sony CMOS Pregius Polarsens sensor (IMX250MZR) a) Camera sensor b) Polarizer array matched to detector pixels c) Unit cell (Super pixel).

Our optical mapping ellipsometer uses a *non-collimated* beam from the monitor screen, unlike conventional ellipsometers that use collimated beams with a well-defined angle of incidence. The concept is based on a patent developed at our institute: Horváth Z Gy, Juhász G, Fried M, Major C, Petrik P: Imaging optical inspection device with a pinhole camera; EP2160591B1, submission number: PCT/HU2008/000058, NSZO: G01N21/8422, country of patent: Europe.

The polarization-sensitive sensor provides the intensity values corresponding to $0°$, $45°$, $90°$, and $135°$ analyzer positions (each for 3 RGB colors). This is fully equivalent to a static rotating-analyzer ellipsometer. The pinhole camera geometry connects each sample point directly to individual pixels, creating an effectively background-free detection system.

The measured area and lateral resolution depend on the distances between monitor–pinhole–sample, and on the pinhole diameter. Currently a 0.2 mm pinhole is used, which is a compromise between detected intensity (1–4 s integration time) and lateral resolution. The lateral resolution is better than 4 mm.

The sample is illuminated by non-collimated light through a fixed polarizer at $45°$. The reflected light passes through a virtual rotating analyzer. Because each camera pixel observes the sample from a different position, and the light arriving at that pixel originates from a different region of the monitor and along a different direction, the illumination exhibits pixel-dependent polarization states. Therefore, these effects must be taken into account during the data evaluation. We describe their combined influence by a multiplicative monitor correction factor, which, for a given measurement configuration, depends only on the camera-pixel position, i.e. on the corresponding position on the sample surface.

Three SiO_2 samples with different thicknesses (nominally 60 nm, 80 nm, and 100 nm) on silicon substrates were used for the calibration process.

In our previous article we used the following calibration procedure [8]: From intensity data of the four polarization states, the ellipsometric angles ψ and Δ can be determined. With three colors available, the camera provides 3 values of ψ and 3 values of Δ. The monitor correction is calculated using the relationship:

$$\rho_{opt}=\rho_{meas}\cdot\rho_{correction}$$

where ρ_{opt} is the ideal value with a perfect light source, ρ_{meas} is the measured value, and $\rho_{correction}$ is the correction factor. We measured three SiO_2-Si samples with different thicknesses and determine $3\cdot N\cdot 2$ values of ψ and Δ (where N=3 wavelengths at present). A full calibration requires to determine:

N real parts of $\rho_{correction}$
N imaginary parts,
3 sample thicknesses,
1 actual angle of incidence for each point.

Thus calibration involves $2\cdot N+3+1$ unknowns. The angle of incidence and the thicknesses depend only on the spatial position, whereas $\rho_{correction}$ depends on both position and wavelength. This makes the correction highly informative about the actual device and optical configuration. The main advantage of the assembly is

that no moving parts in the system! Here, we perform the calibration procedure according to the BPT, see Sec. 3.1.

For validation we used a Woollam M-2000DI Rotating Compensator SE system. The M-2000 SE system with the CompleteEASE software [15] is used to serve the optical properties, layer thicknesses and other related parameters of the sample.

2.2 Theory of ellipsometry

Ellipsometric measurement uses an incident well defined polarization state (polarization state generator, PSG) and after reflection a detection-system which determines the new polarization state (polarization state analyzer, PSA), see Fig. 4. To keep the notation compact, we define the multilayer–optical–model (MLOM) ratio

$$\rho_{MLOM}(\Sigma, \Lambda, \lambda) = r_p(\Sigma, \Lambda, \lambda)/r_s(\Sigma, \Lambda, \lambda), \quad (1)$$

where r_p and r_s are the Fresnel reflection coefficients of the multilayer optical model (MLOM). The parameter sets are

$$\Sigma=\{d_1, \ldots, d_M, n_1, \ldots, n_M\}, \Lambda=\{\theta, P\},$$

where Σ contains the M layer thicknesses and optical constants, and Λ contains the instrument-related quantities (angle of incidence θ and polarizer orientation P). The wavelength λ is not included in Λ, since it enters ρ_{MLOM} explicitly.

Usually, the complex quantity ρ is expressed as

$$\rho=r_p/r_s =tan(\psi)exp(i\Delta) \quad (2)$$

from which the ellipsometric angles follow as

$$\psi(\sum, \Lambda, \lambda)=tan^{-1}(|\rho_{MLOM}(\Sigma, \Lambda, \lambda)|) \text{ and } \Delta(\Sigma, \Lambda, \lambda)=arg(\rho_{MLOM}(\Sigma, \Lambda, \lambda)) \quad (3)$$

In a rotating–analyzer arrangement (see Fig 3 c), the intensity detected after the analyzer is fully determined by the wavelength-dependent Stokes parameters $S_1(\lambda)$ and $S_2(\lambda)$:

$$I(\Sigma, \Lambda, \alpha, \lambda)=I_0(\lambda)[1+S_1(\lambda)cos(2\alpha)+S_2(\lambda)sin(2\alpha)], \quad (4)$$

where $I_0(\lambda)$ is the source spectrum and α is the analyzer orientation.

Because the detector acquires intensity in three broad spectral channels (j = R, G, B), the effective wavelength response is

$SR_j(\lambda)$ = (monitor spectrum)×(camera sensitivity of channel j).

In the following, the index i labels the analyzer orientation, j denotes the spectral channel (R, G, B), and k indexes different sample points (or pixel groups, used in the calibration). The noise-free detector signal is the spectrally integrated model intensity

$$I_{i,j,k}^{raw}(\Sigma_k, \Lambda) = \int I(\Sigma_k, \Lambda, \alpha_i, \lambda) SR_j(\lambda) d\lambda. \quad (5)$$

Both measured and modelled signals are processed in normalized form. To formalize this, we introduce the normalization operator

$$\mathcal{N}[X_{i,j,k}] = \frac{X_{i,j,k}}{\bar{X}_{j,k}}, \bar{X}_{j,k} = \frac{1}{N_\alpha}\sum_{i=1}^{N} X_{i,j,k}, \quad (6)$$

where $N_\alpha = 4$ is the number of analyzer positions.

The normalized model intensities entering the likelihood and calibration pipeline are therefore

$$I_{i,j,k}^{model}(\Sigma_k, \Lambda) = \mathcal{N}\left[I_{i,j,k}^{raw}(\Sigma_k, \Lambda)\right] \quad (7)$$

This compact formulation contains exactly the theoretical elements required for Bayesian inference, calibration of the instrument, and the subsequent determination of the layer parameters. All later sections (Secs. 2.4–2.6 and Sec. 3.1) build directly upon this forward model.

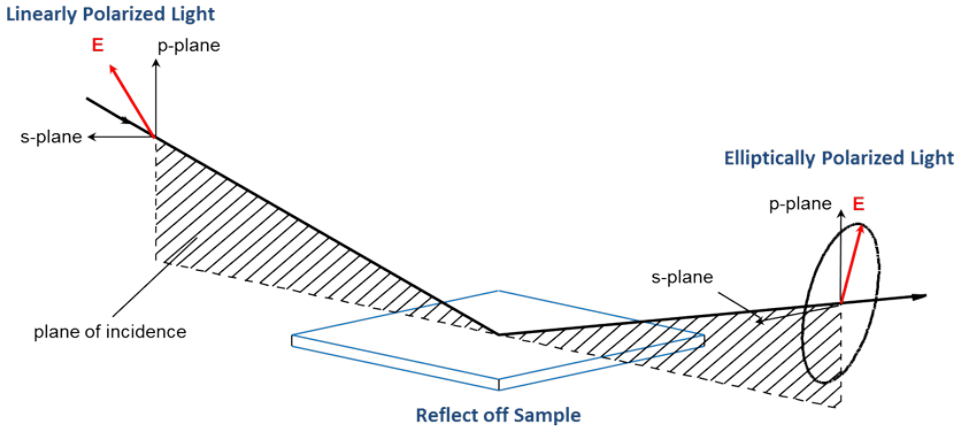

Figure 4. Working principle of spectroscopic ellipsometry
(source: https://www.jawoollam.com/resources/ellipsometry-tutorial/what-is-ellipsometry).

In the case of spectroscopic ellipsometry the light intensity is measured at several wavelengths. Usually, the evaluation means a process where the Σ unknown parameters are changed that way the absolute difference between the measured and calculated $tan\ (\psi)$ and $cos\ (\Delta)$ will be minimized.

2.3 Conventional analysis in spectroscopic ellipsometry

In conventional spectroscopic ellipsometry, the analyzer–dependent intensity measurements are first converted into the Stokes parameters and then, following the relation in eq. 4, the experimental ellipsometric quantities $\rho_{exp}(\lambda_i)$, $tan\ \psi_{exp}(\lambda_i)$ and $cos\ \Delta_{exp}(\lambda_i)$ are obtained.

Conventional spectroscopic ellipsometry works exceptionally well in high–precision commercial instruments because the mechanical stability, angular accuracy and optical quality of the system are extremely high. As a consequence, the experimental configuration (angle of incidence, polarizer and analyzer orientations, beam collimation, spectral response) is very well defined, and the corresponding uncertainties in the model parameters are negligibly small. Under these conditions, the ellipsometric model produces a sharp and well–localized minimum of the merit function, allowing the layer parameters to be determined accurately and uniquely.

The quality of the fit in conventional SE is typically quantified by a Root Mean Square Error (RMSE) function based on the complex ellipsometric ratio:

$$RMSE = \sqrt{\frac{1}{M}\sum_{i=1}^{M}\left|\rho_{exp}(\lambda_i) - \rho_{model}(\Sigma, \lambda_i)\right|^2} \tag{8}$$

Alternative formulations are also used that minimize the separate residuals $tan\ \psi(\lambda_i)$ and $cos\ \Delta(\lambda_i)$ or include an experimental error estimate as weights for the measurands [16].

This approach is highly successful in high–precision ellipsometers, where the optical geometry and spectral response are well controlled and the model parameters are tightly constrained. However, its applicability is limited when only broadband, channel-integrated intensities are available (as in our RGB system), because the quantities ψ and Δ cannot be reconstructed in a physically meaningful way.

2.4 Our Analysis of the ellipsometric data

Why Bayesian Probability Theory is Needed in Our Case?

The RGB optical–mapping ellipsometer differs fundamentally from a conventional spectroscopic ellipsometer. Instead of measuring well-defined monochromatic intensities from which $\psi(\lambda)$ and (λ) can be reconstructed, our instrument records only broadband, wavelength–integrated signals $I_{i,j,k}$ in three wide spectral channels and at four analyzer angles. As a consequence, the Stokes parameters $S_1(\lambda)$ and $S_2(\lambda)$ cannot be recovered, and the conventional mapping $I \rightarrow S_1$, $S_2 \rightarrow \psi$, $\Delta \rightarrow \rho$ breaks down. The quantities reconstructed from such broadband data do not satisfy the multilayer optical model, and numerical tests show that they lead to systematic errors in the inferred layer parameters.

Moreover, the compressed RGB data set provides only limited information: several different combinations of layer thicknesses, effective medium approximated (EMA) compositions, instrument offsets and angle-of-incidence values can reproduce the measured intensities within the noise. This produces strong parameter correlations and a merit function that is broad or multimodal, so that a least-squares estimate is not guaranteed to correspond to the physically most probable solution.

Bayesian Probability Theory (BPT) is therefore essential. The posterior (where D is the data set, $\mathcal{L}$ is the likelihood and π is the prior):

$$P(\Sigma, \Lambda|D) \propto \mathcal{L}(D|\Sigma, \Lambda)\pi(\Sigma, \Lambda) \quad (9)$$

allows us to incorporate well-motivated priors (realistic thickness ranges, composition constraints, analyzer-angle limits, smoothness of instrumental corrections) and provides a statistically consistent treatment of uncertainty. Marginalization over nuisance parameters yields credible intervals and parameter correlations that cannot be obtained reliably with classical methods.

Finally, our complete evaluation pipeline is inherently Bayesian: instrument-specific correction parameters are inferred first and reused as priors when analyzing additional samples. Such sequential learning is a natural feature of BPT and cannot be reproduced by conventional ellipsometric inversion. For these reasons Bayesian inference is not merely advantageous, but *necessary* for the reliable evaluation of broadband RGB optical–mapping ellipsometry.

Bayesian Probability Theory for Parameter Estimation

This section summarizes the key concepts of Bayesian Probability Theory (BPT) relevant to parameter estimation and uncertainty quantification in inverse problems.

BPT is commonly applied to two distinct classes of inference problems: hypothesis testing (or model selection) and parameter estimation. In hypothesis testing, the goal is to compare different competing models and to assign posterior probabilities to them given the data. In contrast, parameter estimation assumes a fixed forward model and focuses on inferring the numerical values of its unknown parameters together with their uncertainties and correlations.

In the present work, the physical structure of the sample and the optical forward model are assumed to be known *a priori*. The main objective is therefore not to discriminate between alternative models, but to determine continuous parameters such as layer thicknesses, effective optical constants, and instrumental parameters from noisy RGB intensity measurements. Consequently, the Bayesian framework is employed here in the form of parameter estimation rather than model selection.

The unknown parameters are collected into a parameter vector Θ (Σ and Λ), $\mathbb{D}$ is the measured data set, and the solution of the inverse problem is given by the posterior probability distribution

$$P(\Theta|D) \propto \mathcal{L}(D|\Theta)\pi(\Theta) \quad (10)$$

where $\mathcal{L}$ is the likelihood function linking the measured RGB intensities to the forward model, π is the prior denotes the prior distribution encoding independent physical constraints.

The posterior $P(\Theta|D)$ is defined over all optical and instrumental parameters. For a single parameter of interest θ_k, Bayesian marginalization gives

$$P(\theta_k|D) = \int P(\Theta|D)d\theta_1 \dots d\theta_{k-1}d\theta_{k+1} \dots d\theta_p \quad (11)$$

For $\Theta = (\Sigma, \Lambda)$ this yields credible intervals and parameter correlations even when the inverse problem is underdetermined.

The prior $\pi(\Theta)$ introduces physically motivated parameter constraints. Realistic layer-thickness ranges, admissible compositions, analyzer-angle limits, and bounds implied by RGB spectral integration are all encoded in $\pi(\Sigma, \Lambda)$, preventing unphysical solutions and stabilizing the inference.

The light source of our system (the LCD monitor) is not an ideal polarization–state generator: its emitted polarization depends on both the spatial position on the screen and the wavelength. As a consequence, the polarization state incident on the sample varies across the field of view and cannot be described by a single, global set of instrumental parameters.

For this reason, the data–analysis strategy must explicitly account for instrument–specific distortions. In particular, the calibration procedure has to determine a polarization–state correction map $\rho_{monitor}(x, y, \lambda)$ over the entire field of view. In parallel, an angle–of–incidence (AOI) calibration must be performed, which assigns each CMOS pixel (or pixel group) to its corresponding local angle of incidence. If these effects are not known, the physical layer parameters of the sample cannot be determined in a meaningful or reliable way.

The first step of the analysis strategy is therefore the explicit incorporation and determination of these disturbing instrumental effects within the forward model. This step is referred to as the calibration of the measurement system. The calibration is carried out using measurements performed on a set of well–characterized reference samples.

The outcome of this first step is a set of calibration parameters, together with their associated uncertainties, which characterize the actual optical behavior of the measurement system. In the second step, these calibration parameters are used as fixed or probabilistically constrained inputs for the evaluation of unknown samples. In this way, the physical layer parameters of real samples are determined while consistently accounting for the previously inferred instrumental corrections.

Before applying this two–step strategy to experimental data, numerical experiments are performed on synthetic data sets. These simulations make it possible to validate the analysis workflow, to study parameter correlations and degeneracies, and to assess the interpretability and expected accuracy of the results obtained from real measurements.

2.5 Bayesian Determination of Instrumental and Layer Parameters

The objective of the Bayesian evaluation is to determine the instrumental correction parameters Λ and the physical layer parameters Σ from the measured RGB intensity data. The complete parameter vector is denoted by Θ (Σ, Λ), and the predicted normalized intensities are denoted $I_{i,j,k}^{model}(\Theta)$, where the indices i, j, and k refer to analyzer position, spectral channel, and number of sample, respectively

Assuming independent Gaussian noise with variance σ^2 for the normalized intensity signals, the likelihood function is given by

$$\mathcal{L}(D|\theta) \propto e^{\left[\frac{-1}{2\sigma^2}\sum_{i,j,k}\left(I_{i,j,k}^{measured} - I_{i,j,k}^{model}(\theta)\right)^2\right]} \quad (12)$$

Within the Bayesian framework, the solution of the inverse problem is expressed by the posterior probability distribution

$$P(\theta|D) \propto \mathcal{L}(D|\theta)\pi(\theta) \quad (13)$$

where $\pi(\theta)$ denotes the prior distribution encoding independent physical and instrumental constraints. and maximizing it is equivalent to minimizing

$$\chi^2(\theta) = \sum_{i,j,k}\left(I_{i,j,k}^{measured} - I_{i,j,k}^{model}(\theta)\right)^2 \quad (14)$$

The most probable parameter vector (MAP) is defined as the maximum a posteriori estimate

$$\theta_{MAP} = argmax\ P(\theta|D)$$

If uniform (flat) priors are assumed over the relevant parameter ranges, maximizing the posterior is equivalent to minimising the corresponding χ^2 objective function:

$$\theta_{MAP} = argmin\chi^2(\theta)$$

In the general case, however, the MAP estimate explicitly reflects both the likelihood and the prior information.

The determination of parameter uncertainties and correlations is based on the local and marginalized structure of the posterior distribution around θ_{MAP}. This allows credible intervals and parameter correlations to be obtained in a statistically consistent manner.

In the practical evaluation workflow, the same likelihood formulation is used for both the calibration and the analysis of unknown samples, while the parameter sets and prior distributions differ. During the calibration step, the instrumental parameters Λ are treated as unknowns and inferred from measurements on

well–characterized reference samples, whereas the corresponding layer parameters are constrained by narrow priors. In contrast, during the evaluation of polycrystalline silicon samples, the previously inferred calibration parameters are incorporated as informative priors for Λ, and the physical layer parameters Σ become the primary quantities of interest.

In the subsequent sections, the general Bayesian framework introduced here is applied to the two main stages of the evaluation workflow. In the calibration stage, described in Sec. 3.1, the explicit likelihood functions and prior distributions are specified for the determination of the instrumental correction parameters using well–characterized SiO_2-Si reference samples. In a separate, subsequent section, the Bayesian determination of the layer structure of polycrystalline–silicon samples is addressed, where the previously inferred calibration parameters enter the analysis as informative priors.

For both stages, the definition of the likelihood, the choice of prior distributions, and the post–processing of the resulting posterior distributions are discussed in detail. This includes the extraction of MAP estimates, the determination of parameter uncertainties and correlations, and the interpretation of the results in terms of the physical layer structure of the samples

Overview of the analysis workflow

The main stages of the data–analysis procedure implemented in this work are summarized as follows:

***Forward modelling**: calculation of normalised RGB intensities from the multilayer optical model, where the ideal ellipsometric response is augmented by instrumental correction factors. Specifically, the monitor–correction function $\rho_{monitor}(x, y, \lambda)$ and the local angle–of–incidence parameters are incorporated directly into the forward model, followed by spectral integration over the R, G, and B channels.*
***Bayesian formulation of the inverse problem**: explicit construction of the likelihood function linking the measured RGB intensities to the forward model, and definition of prior distributions reflecting physical constraints and prior knowledge of the model and instrumental parameters.*
***Noise estimation**: determination of a global intensity uncertainty parameter σ from a sinusoidal fit to the measured intensities, used exclusively to define the width of the likelihood function.*
***Bayesian calibration**: joint inference of the monitor–correction function ρ_monitor (x,y,λ) and the local angle–of–incidence map using well–characterised SiO_2-Si reference wafers. The maximum of the resulting posterior distribution is first located by a most probable parameter vector (MAP) estimate obtained using simulated annealing, after which the calibration parameters are marginalized and reformulated as informative priors for the subsequent sample analysis.*
***MAP estimation**: localization of the maximum of the posterior distribution by computing the maximum a posteriori (MAP) estimate of the calibration parameters using a simulated annealing (SA) algorithm.*
***Sample analysis**: Bayesian evaluation of samples not used in the calibration stage, including both polycrystalline–silicon (poly–Si) on SiO_2-Si structures and additional SiO_2-Si wafers with oxide thicknesses outside the calibration set. The calibrated instrumental parameters are incorporated as informative priors, while the physical layer parameters of the samples are inferred from the measured RGB intensities.*
***Posterior analysis**: extraction of credible intervals and parameter correlations, propagation of calibration uncertainties, and assessment of the robustness and limitations of the measurement.*

Determination of uncertainty

The calibration step determines several instrumental and sample-related quantities simultaneously, including the wavelength–dependent monitor–correction parameters, the angle–of–incidence map, and the oxide thicknesses of the reference wafers. These parameters jointly influence the measured broadband RGB intensities and therefore exhibit strong correlations in the posterior distribution. Since the calibration parameters are subsequently used as priors in the evaluation of all other samples, their uncertainties and covariance propagate through the entire data–analysis pipeline.

Within the Bayesian framework, the accurate determination of the measurement uncertainty of the raw detector signals is therefore a central element of the inference problem. The noise level directly sets the width of the likelihood function and thereby controls the shape of the posterior distribution. As a consequence, it determines not only the uncertainties of the calibration parameters themselves, but also their mutual correlations and, through prior propagation, the uncertainties of the layer parameters extracted for all unknown samples. An underestimation or overestimation of the noise level would lead to unrealistically narrow or artificially broad posterior distributions, respectively, and would bias the entire Bayesian inference chain.

To estimate the statistical uncertainty, a sinusoidal model—derived from classical rotating–analyzer ellipsometry—is fitted to the measured intensities at each wavelength position. This model is used only for noise estimation and is not employed in the RGB intensity–based inversion. The purpose of this fit is not to provide a physical forward model, but to obtain a realistic estimate of the measurement uncertainty. In addition to describing the statistical fluctuations of the detected signals, the deviation of the measured data from the fitted sinusoidal model also reflects systematic mismatches between the experimental intensities and an idealized model response. Consequently, the estimated uncertainty incorporates not only pure detector and photon noise, but also the stochastic component of model imperfections that cannot be described explicitly in the RGB intensity–based inversion. For each wavelength λ_i and analyzer angle α_j the fitted model is

$$I_{fitted}(\lambda_i,\alpha_j) = I_0(\lambda_i)\left[1 + \alpha(\lambda_i)sin(2\alpha_j) + \beta(\lambda_i)cos(2\alpha_j)\right],$$

where $I_{fitted}(\lambda_i,\alpha_j)$ is the fitted, $I_{measured}(\lambda_i,\alpha_j)$ is the measured intensity, and $I_0(\lambda_i)$, $\alpha(\lambda_i)$, $\beta(\lambda_i)$ are the three fitted parameters.

The residual measurement error is defined as

$$\delta_{i,j} - I_{measured}(\lambda_i,\alpha_j) - I_{fitted}(\lambda_i,\alpha_j),$$

and a relative (normalized) deviation is computed as

$$\delta_{i,j}^{I/I_0} = \frac{I_{measured}(\lambda_i,\alpha_j) - I_{fitted}(\lambda_i,\alpha_j)}{I_0(\lambda_i)},$$

Since the distribution of $\delta_{i,j}^{I/I_0}$ is approximately normal with zero mean, its standard deviation is estimated as

$$\sigma_{I/I_0} = \sqrt{\frac{1}{N_{DF}}\sum_{i,j}(\delta_{i,j}^{I/I_0})^2},$$

where N_{DF}=*M-3* is the number of degrees of freedom (three fitted parameters at each λ_i), corresponding to the three fitted parameters at each wavelength. In practice, this wavelength–dependent variance is averaged over the entire sample area, and a single global noise parameter σ_{I/I_0} is used in the likelihood evaluation.

In our measurements, the resulting uncertainty of the normalized RGB intensities is typically on the order of ~2 %, and this value enters the likelihood function directly as σ. Finally, we note that the uncertainty determined in this way contains not only statistical fluctuations of the detected light but also additional stochastic contributions such as surface–scattering effects, microscopic thickness or composition variations, and other instrument-dependent noise sources. These effects propagate through the Bayesian calibration and ultimately influence both the uncertainties and the correlations of the inferred layer parameters for all measured samples.

2.6 One example of fitting procedure

In this section, a representative example is shown to illustrate the parameter–estimation procedure applied to a single measurement point on a polycrystalline–silicon layer on silicon dioxide (poly-Si-SiO_2) sample. For this type of sample, only the thicknesses of the poly–Si and SiO_2 layers need to be determined, while the instrumental correction parameters are provided by the preceding calibration step.

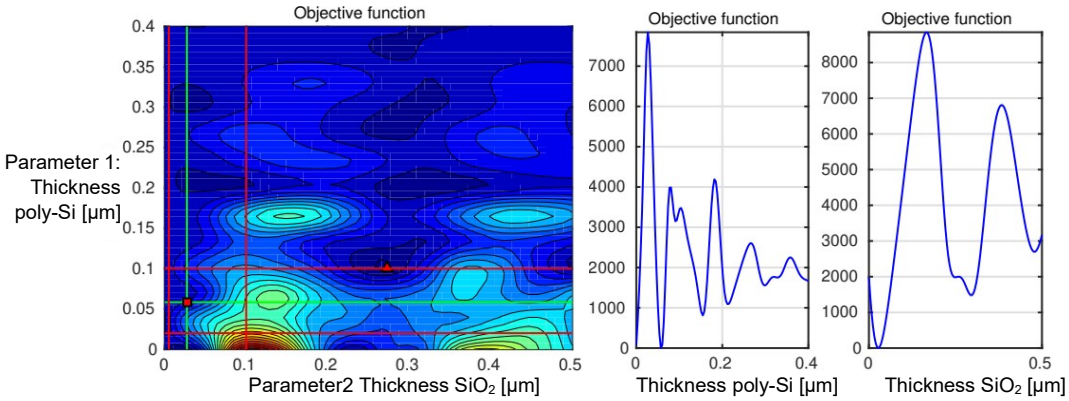

Figure 5. The "Objective function" map (left) shows the χ^2 (Eq. 14) values in the parameter space (Parameter1 is the thickness (in micron) of the poly-Si layer, Parameter2 is the thickness (in micron) of SiO_2 layer) The real global minimum is at the cross-point of the green lines (red spot). Red lines show the ranges designated by the priors. The objective function values along the green lines are shown in the right part of the Figure.

Due to the broadband RGB nature of the measurement and the nonlinear dependence of the measured intensities on the model parameters, the objective function exhibits a complex structure with multiple local minima. This behavior is visualized in Fig. 5, which shows the objective–function values (Eq. 14) evaluated on a two–dimensional grid spanned by the poly–Si and SiO_2 layer thicknesses.

The presence of several local minima demonstrates that deterministic gradient–based optimization alone is insufficient, as it would generally converge to a local minimum depending on the initial guess. Within the Bayesian framework, this problem is addressed by locating the maximum of the posterior distribution using a global optimization strategy based on simulated annealing (SA)

In Figure 5, the range of thickness (in micron) values was chosen to be large. It can be seen that the objective function contains many local minima. It can also be observed that some local minima, as well as one global minimum, do not correspond to physically meaningful layer parameters for the sample. In the left part of Figure 5, the ranges bounded by red lines indicate the domains where the sample's layer thickness values can lie. During the Bayesian evaluation, we will use values along the green lines as the prior for the layer thickness.

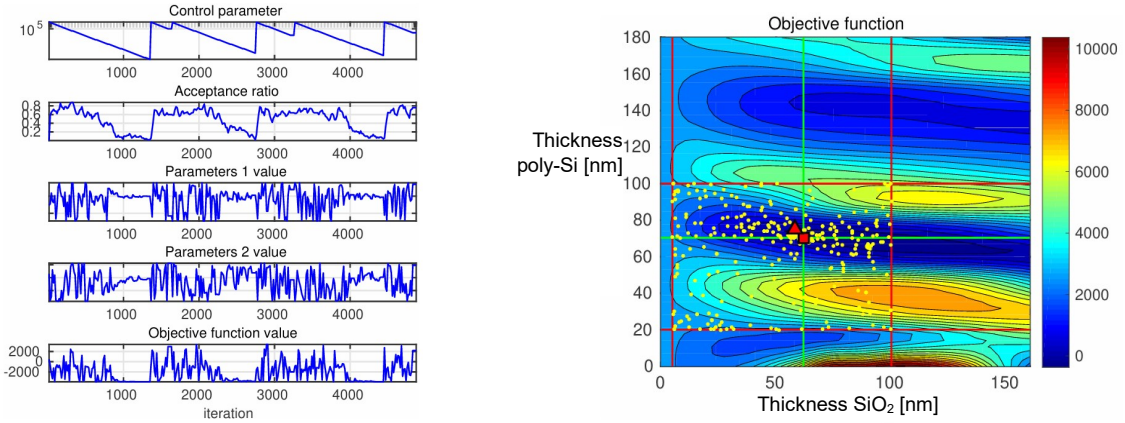

Figure 6. The course of the Simulated Annealing fitting process (left). (Control parameter is the Temperature.) The real global minimum is at the cross-point of the green lines (red spot). Red lines show the ranges designated by the priors. The yellow spots are the tried thickness-pairs.

Fig. 6 illustrates the course of the SA [17] optimization for this example. During the annealing process, the algorithm explores the parameter space broadly at high temperatures and gradually focuses on the region of

the global minimum as the temperature is reduced. The final solution corresponds to the maximum a posteriori (MAP) estimate of the parameter vector.

After the MAP estimate has been obtained, the corresponding forward model is evaluated and compared directly with the measured camera signals. Fig. 7 shows the measured and fitted intensity values in the three RGB wavelength ranges. The agreement confirms that the inversion is performed directly on the measured intensity signals rather than on derived ellipsometric quantities.

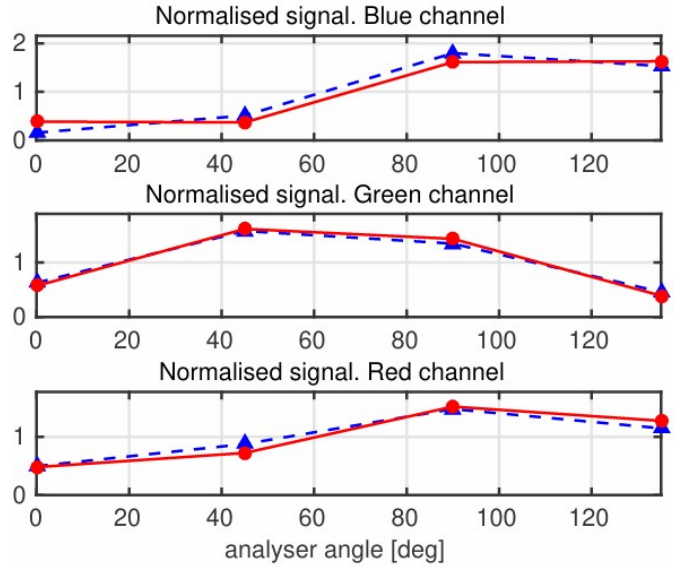

Figure 7. Camera signals in the three wavelength ranges. Blue triangles: the measurement data. Red diamonds: the best fit.

For comparison only, the corresponding tan ψ and cos Δ values derived from the camera signals are shown in Fig. 8. These quantities are *not* used in the inversion procedure and are displayed solely to illustrate the relation between the intensity–based approach and conventional spectroscopic ellipsometry.

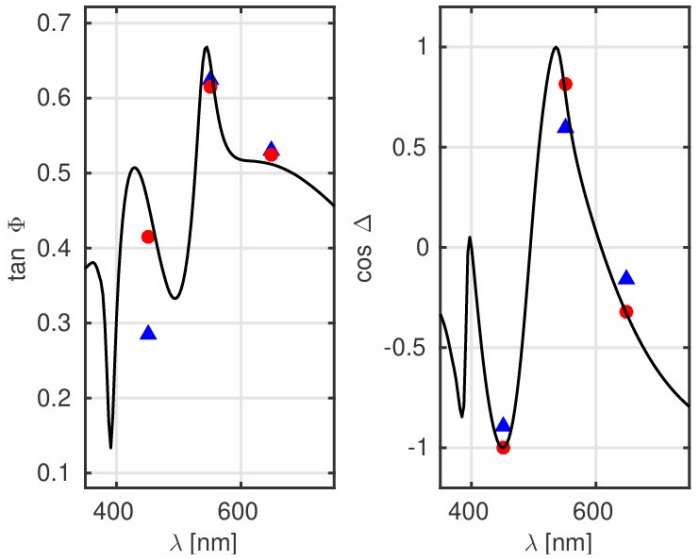

Figure 8. The values of tan ψ and cos Δ calculated from the camera signals, in three wavelength ranges and from the four polarization angles, are shown as blue triangles at the center of the wavelength ranges. The same values calculated from the fitted data are shown as red circles. The black curve represents these values across the entire wavelength range. Note that the fitted values do not need to fall on the continuous curve, as during the evaluation we do not use the tan ψ and cos Δ values, but rather the camera signals, see Figure 7.

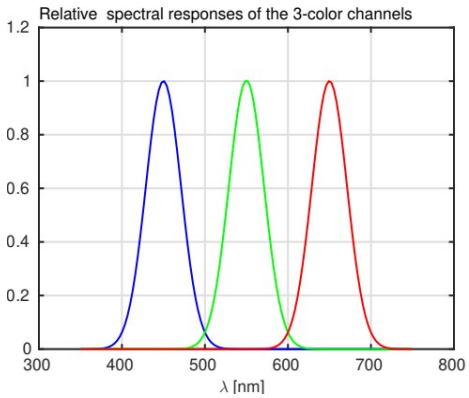

Figure 9. The spectrum of the monitor combined with the sensitivity of the camera. This function serves to determine the camera signal in the three (RGB) wavelength ranges in the applied model function.

Finally, Fig. 9 shows the combined spectral response of the monitor and the camera, which defines the effective wavelength weighting of the RGB channels in the forward model. This function is used both for the calculation of the predicted intensities and for the estimation of the measurement noise.

This example demonstrates that the inverse problem associated with broadband RGB ellipsometric mapping is intrinsically non–convex and cannot be solved reliably using local optimisation alone. The combination of Bayesian inference with simulated annealing enables robust identification of the global optimum and provides a consistent framework for subsequent uncertainty quantification.

3. Results

3.1 Calibration of the instrument

The light source (the monitor) in the system is not an ideal polarization–state generator: its emitted polarization depends on both the spatial position on the screen and the wavelength in a nonlinear manner [8]. For this reason, the calibration procedure must determine a polarization–state correction map $\rho_{monitor}(x, y, \lambda)$ over the entire field of view. In parallel, an angle–of–incidence (AOI) calibration must be performed, which assigns each CMOS pixel (or pixel group) to its corresponding local angle of incidence. Calibration is carried out using well–characterized optical reference samples.

The calibration samples are 20 cm diameter crystalline silicon (c-Si) wafers having different thicknesses of thermal oxide (SiO_2), nominally 60, 80, 100 nm thick SiO_2 layers. These samples provide reliable and sufficiently distinct ellipsometric responses to constrain the device–specific instrumental correction terms.

The monitor–correction factor enters the optical model multiplicatively through the complex reflection ratio,

$$\rho_{model}(\Sigma, \Lambda, \lambda) = \rho_{MLOM}(\Sigma, \Lambda, \lambda) \cdot \rho_{monitor}(x, y, \lambda),$$

where x and y denote the position on the sample surface.

A smooth parameterization of $\rho_{monitor}$ is required to ensure numerical stability and physical consistency. For each pixel (or pixel group), the real and imaginary parts of the correction factor are represented by second–order polynomials in wavelength,

$$\Re(\rho_{monitor}) = a_0 + a_1\lambda + a_2\lambda^2, \Im(\rho_{monitor}) = b_0 + b_1\lambda + b_2\lambda^2.$$

For clarity of presentation, the polynomial coefficients are quoted in later sections at the average wavelengths of the R, G, and B channels. This allows a compact and physically intuitive representation of the calibration parameters without altering their role in the forward optical model.

The calibration is not performed on individual pixels, but on pixel groups whose size is chosen to match the nominal lateral resolution of the system.

In Sec. 2.2 *Theory of Ellipsometry*, the theoretical ellipsometric ratio $\rho_{MLOM}(\Sigma_k, \Lambda, \lambda)$ was introduced based on the multilayer optical model (MLOM). During the calibration procedure, this quantity is extended to include the instrumental correction of the light source, yielding the effective optical response

$$\rho_{opt}(\lambda) = \rho_{MLOM}(\Sigma_k, \Lambda, \lambda) \cdot \rho_{monitor}(\lambda),$$

where $\rho_{monitor}(\lambda)$ is understood for a given pixel or pixel group.

The corrected optical response $\rho_{opt}(\lambda)$ determines the Stokes-vector components $S_1(\lambda)$ and $S_2(\lambda)$ appearing in the rotating–analyzer intensity formulation. By inserting $\rho_{opt}(\lambda)$ into the expressions for $S_1(\lambda)$ and $S_2(\lambda)$ given in Sec. 2.2, and subsequently into the spectral integration

$$I_{i,j,k}^{raw}(\Sigma_k, \Lambda) = \int I(\Sigma_k, \Lambda, \alpha_i, \lambda) S R_j(\lambda) d\lambda,$$

the complete intensity–based forward model used during the calibration is obtained.

Within this framework, the calibration procedure determines simultaneously:

-the physical layer parameters of the calibration wafers (Σ_k),
-the angle–of–incidence related instrumental parameters (Λ),
-and the wavelength–dependent monitor–correction factor $\rho_{monitor}(\lambda)$,

through a unified Bayesian optimization.

For all three calibration samples, the predicted normalized intensities $I_{i,j,k}^{model}(\Sigma_k, \Lambda, \rho_{monitor})$ are used to construct the likelihood function in the Bayesian analysis. The oxide thickness values obtained from a high–precision commercial spectroscopic ellipsometer (Woollam M–2000DI) serve as informative priors for the oxide layer thicknesses. Since the same monitor–correction function is assumed to apply over the entire sample surface, uninformative (flat) priors are adopted for the corresponding instrumental correction parameters, allowing for spatial variations of the oxide thickness across the wafer.

By combining the forward model and the prior information, the posterior distribution

$$P(\Sigma_k, \Lambda, \rho_{monitor}|D) \propto \mathcal{L}(D|\Sigma_k, \Lambda, \rho_{monitor}) \pi(\Sigma_k, \Lambda, \rho_{monitor})$$

is evaluated, and the most probable values of the calibration parameters are determined.

The prior distributions reflect the different levels of prior knowledge available for the calibration parameters. For the SiO_2 reference wafers, the oxide thicknesses are assigned narrow, approximately flat priors centred on the nominal values, consistent with the independent thickness measurements obtained by commercial spectroscopic ellipsometry. These priors allow for small thickness variations across the wafer while preventing unphysical solutions.

In contrast, for the instrumental parameters, including the angle–of–incidence and the parameters of the monitor–correction function $\rho_{monitor}(\lambda)$, flat (non–informative) priors are employed over physically meaningful parameter ranges. This choice reflects the absence of detailed *a priori* knowledge of the instrumental distortions while ensuring that the inferred parameters remain within realistic bounds.

The Bayesian formulation of the calibration problem has an important consequence: there is no fundamental restriction on the number of calibration samples used in the procedure. Any number of well-characterized reference wafers may be included in the joint inference

$$P(\Sigma_k, \Lambda, \rho_{monitor}|D) \propto \mathcal{L}(D|\Sigma_k, \Lambda, \rho_{monitor}) \pi(\Sigma_k, \Lambda, \rho_{monitor}),$$

because each additional calibration sample contributes an additional likelihood factor, thereby refining the inferred parameter distributions.

Consequently, the accuracy of the inferred calibration parameters (the six polynomial coefficients describing $\rho_{monitor}(\lambda)$, the angle-of-incidence map, and the oxide thicknesses of the reference wafers) systematically improves as the number of calibration samples increases. With more samples, the likelihood becomes more constrained and the parameter uncertainties are reduced, while the priors ensure physical consistency.

3.2 Results of Calibration

3.2.1 Full area calibration

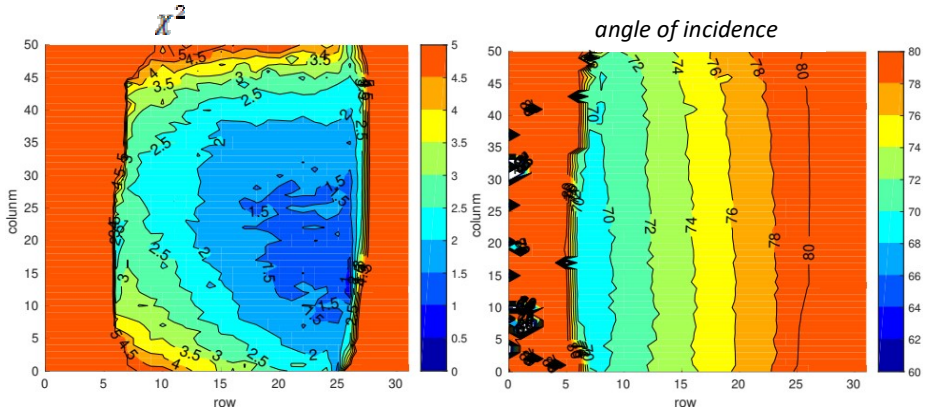

Figure 10. Full χ^2 map (left) and calibrated angle of incidence map (right). The full frame is: 30x30 cm, X-direction: 1-50 columns; Y-direction: 1-30 rows.

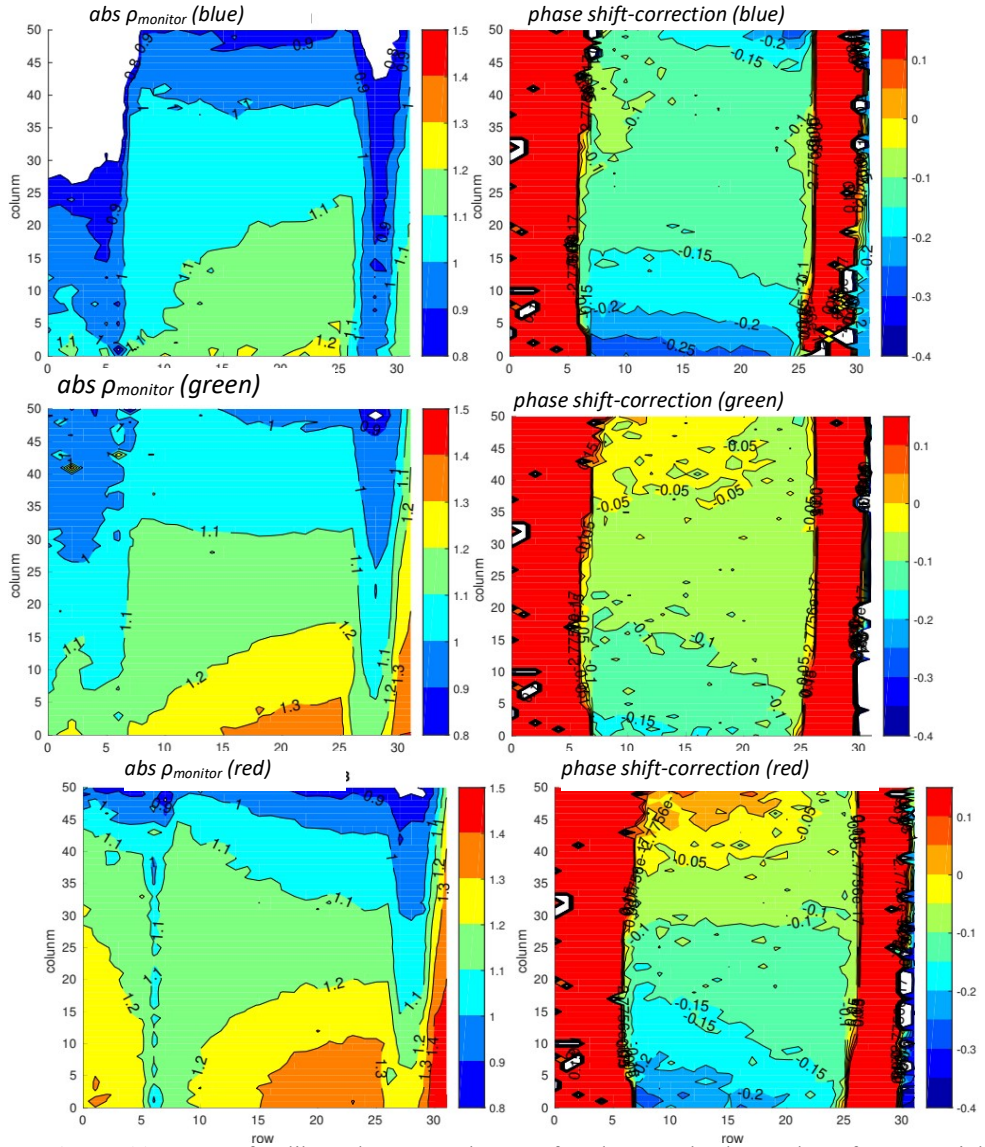

Figure 11. Maps of calibrated $\rho_{monitor}$ values. Left columns: absolute value of $\rho_{monitor}$; right columns: phase shift-correction maps. Upper row: blue (450 nm) color band; Middle row: green (550 nm) color band; Lower row: red (650 nm) color band. The full frame is: 30x30 cm, X-direction: 1-50 columns; Y-direction: 1-30 rows.

As a first step, the calibration procedure was applied to the entire camera field of view. The full frame is: 30x30 cm, X-direction: 1-50 columns; Y-direction: 1-30 rows. The results can be seen in Fig. 10-12: the χ^2 map, the angle of incidence map, the $\rho_{monitor}$ maps, the thickness maps of SiO_2/Si samples with nominal thickness of 60 nm, 80 nm, and 100 nm.

The wavelength-dependent monitor-correction factor maps obtained from the calibration procedure are shown in Fig. 11. Both the absolute value and the phase of $\rho_{monitor}$ are displayed. For clarity, the result is shown explicitly for the blue channel (approximately 450 nm); the corresponding maps for the green (550 nm) and red (650 nm) channels exhibit similar behavior. The inferred angle-of-incidence map (Fig. 10 right) follows the behavior expected from the experimental geometry. The monitor-correction factors (Fig. 11) are smooth and exhibit relatively small deviations (with absolute values close to unity and phases close to zero), indicating that the calibration compensates moderate but systematic deviations of the optical response.

The same calibration process resulted in the thickness maps of our calibration oxide samples (nominal thickness of 60, 80, and 100 nm), which are shown in Figure 12.

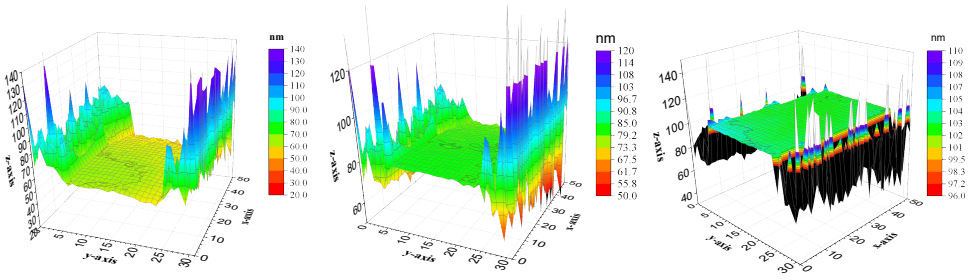

Figure 12. Thickness maps of SiO_2/Si samples with nominal thickness of 60 nm, 80 nm, and 100 nm. The central 20 × 15 cm part is valid.

The calibration results obtained over the full camera field of view clearly demonstrate that the validity of the measurement and evaluation model is not uniform across the image. While the Bayesian calibration framework is capable of inferring instrument- and sample-related parameters simultaneously, its physical and statistical reliability depends on the quality and consistency of the measured data. One can see from the χ^2 map (Fig. 10) that the region where the calibration is valid only at the central part, where the measuring conditions are good. (Calibration sample is smaller than the camera viewed area and the intensity is not enough everywhere.) The χ^2 values are too high, and the angle of incidence map is not smooth at the edges. So, a narrower (valid) area can be used for the other measurements, see Fig. 13 and 14. This valid area is the central 20x15 cm, X-direction: 5-40 columns; Y-direction: 8-24 rows.

3.2.2 Valid area calibration

Not only the values of the calibration parameters are important, but also their uncertainties, since these uncertainties propagate directly into the subsequent analysis of the polycrystalline silicon samples. The uncertainties of the inferred calibration parameters originate from both systematic and statistical error sources. These contributions are explicitly taken into account in the subsequent analysis and define the limits of the achievable accuracy of the method. Systematic errors are primarily related to the measurement system and the calibration procedure. They include uncertainties in the effective polarization states of the illumination, as well as imperfect knowledge of the analyzer and polarizer angles.

An additional source of systematic uncertainty originates from the spectral response functions $SR_j(\lambda)$ of the RGB channels. These functions are not known exactly and are therefore approximated by Gaussian functions. The associated uncertainties enter the forward model through the parameters describing the center wavelength and the spectral width of the Gaussian profiles, and they propagate into the inferred calibration parameters via the model evaluation.

Statistical errors arise mainly from sample-related effects. These include spatial variations of the SiO_2 layer thickness across the surface of the calibration wafers, as well as local variations of surface properties such as surface roughness. Such effects introduce spatially varying deviations in the measured intensities and contribute to the statistical spread of the inferred parameters.

Taking the considerations of the previous paragraphs into account, a quadratic surface was fitted to the calibration parameters within the valid area. This fitted surface acts as a spatial smoothing of the calibration

parameter maps. When using the values obtained from this smooth quadratic surface for the analysis of the polycrystalline silicon samples, the contribution of the statistical uncertainty of the calibration parameters becomes negligible compared to other sources of uncertainty. Within the Bayesian framework, this is reflected by omitting the statistical variance term associated with these calibration parameters from the prior distribution used in the subsequent analysis.

The resulting calibration maps together with the fitted quadratic surfaces are shown in Fig. 13 and 14. The parameter correlations obtained from the inverse analysis reveal a strongly coupled parameter space. Several pairs of parameters exhibit correlation coefficients with magnitudes exceeding 0.6, indicating that different combinations of layer parameters, instrumental quantities, and correction factors can reproduce the measured RGB intensities with comparable accuracy.

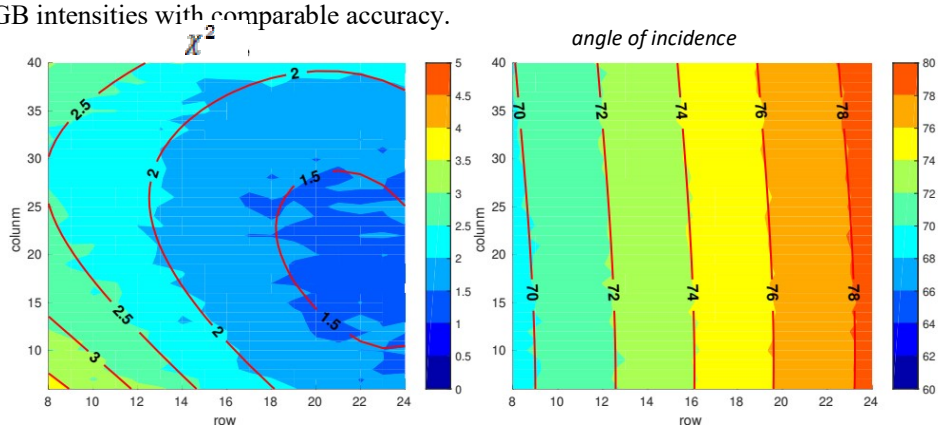

Figure 13. χ^2 map (left) and angle of incidence map (right) on the valid area. The full frame is: 30x30 cm, X-direction: 1-50 columns; Y-direction: 1-30 rows.

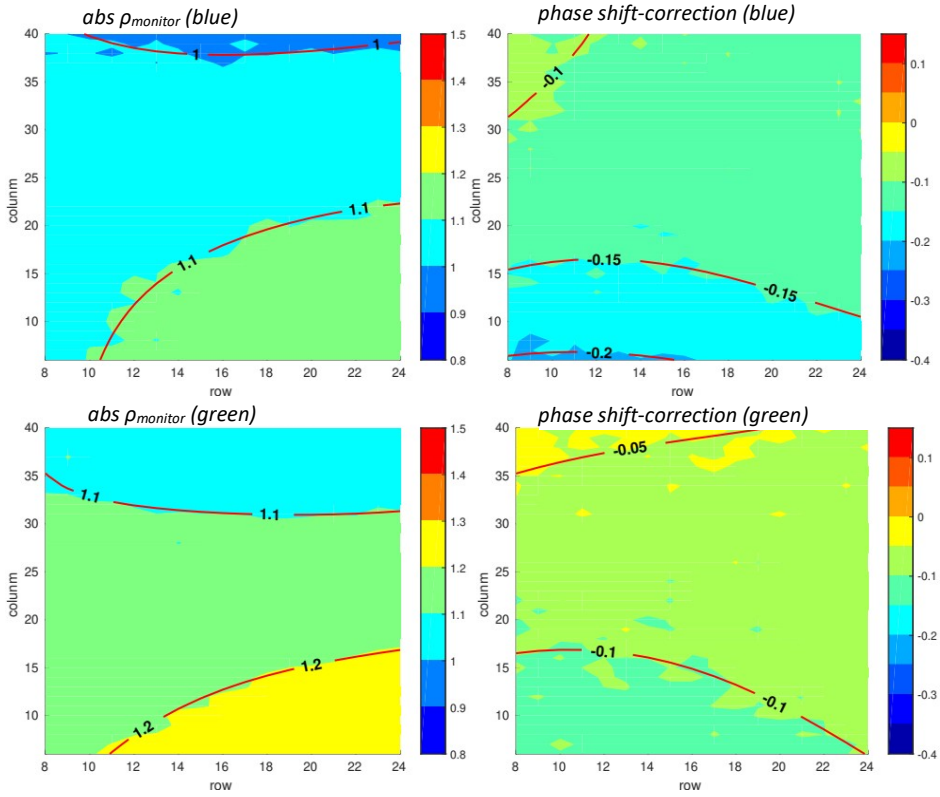

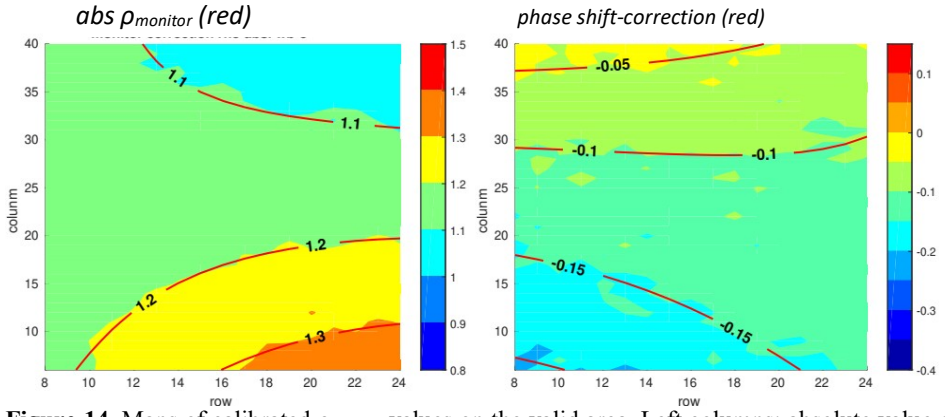

Figure 14. Maps of calibrated $\rho_{monitor}$ values on the valid area. Left columns: absolute value of $\rho_{monitor}$; right columns: phase shift-correction maps. Upper row: blue (450 nm) color band; Middle row: green (550 nm) color band; Lower row: red (650 nm) color band. The full frame is: 30x30 cm, X-direction: 1-50 columns; Y-direction: 1-30 rows.

We estimated the scattering of the instrument calibration parameters, which we obtained by taking the difference between the calibrated parameters and the smoothed calibrated parameters. From these distributions, the statistical error of the calibration parameters can be determined, which we used later to determine the error of the layer parameters of the other samples, see later.

The standard deviation of abs($\rho_{monitor}$) and phase shift-correction values are around ±0.01, and 0.11 degree in the case of angle of incidence, see Fig. 15.

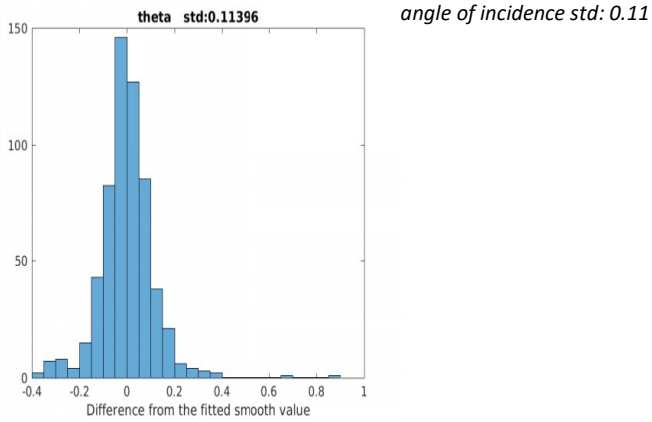

Figure 15. Difference of the calibrated angles of incidence (see Fig. 13) values from the fitted smoothed value. The standard deviation is 0.11 degree.

3.3 Validation measurements

The purpose of this section is not to validate the measurement itself. Within the valid area we assume the measured RGB intensities to be reliable. Instead, we validate the complete evaluation pipeline, i.e. the sequence

$$\text{calibration data} \rightarrow P(\Lambda, \rho_{monitor} \mid D_{cal}) \rightarrow$$
$$\text{informative prior for subsequent samples} \rightarrow P(\Sigma \mid D_{sample}),$$

and we test whether the inferred calibration parameters can be reused consistently in the analysis of independent samples.

To validate the calibration procedure and its use in subsequent sample analysis, independent measurements were performed on two SiO_2/Si wafers that were *not* involved in the calibration step. Both samples had a diameter of 20 cm and nominal oxide thicknesses of 20 nm and 120 nm, respectively. The calibrated monitor–correction function $\rho_{monitor}(x,y,\lambda)$ and the angle–of–incidence map obtained from the Bayesian calibration were applied to the measured RGB intensity data. Using these corrected intensities, oxide–thickness maps were determined with the Bayesian inversion procedure described in the previous sections. In this way, the calibration posterior is reused as an informative prior for the analysis of independent samples.

For reference, the same wafers were measured using a commercial Woollam M–2000 spectroscopic ellipsometer. Due to the geometrical constraints of the M–2000 system, only the central 14 cm diameter region of the 20 cm wafers could be mapped. Therefore, a strict point–by–point comparison over the full wafer area is not possible.

The thickness maps of the oxide samples in Fig. 16 b) and 17 b) appears to be smooth enough. Note that one color in Fig. 16 and 17 is only 0.5 nm or 1 nm which corresponds to one or two atomic layers.

Within the overlapping measurement area, the agreement between the oxide–thickness values obtained with the present RGB ellipsometric mapping system and those measured by the Woollam M–2000 ellipsometer is typically better than 1 nm for both samples. Considering the broadband RGB integration, the non–collimated illumination geometry, and the different lateral resolutions of the two systems, this level of agreement demonstrates that the calibration posterior can be reused consistently in the Bayesian analysis of independent samples.

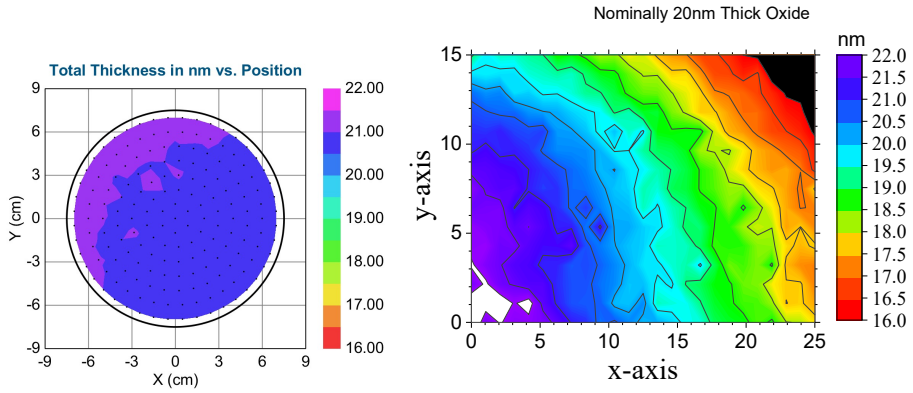

Figure 16. Thickness maps from a nominally 20 nm thick oxide film on a 20 cm diameter Si-wafer. a) Woollam M2000 ellipsometer b) our device from cheap parts. (Note that our M2000 can map only the central 14 cm diameter area of the 20 cm diameter sample.).

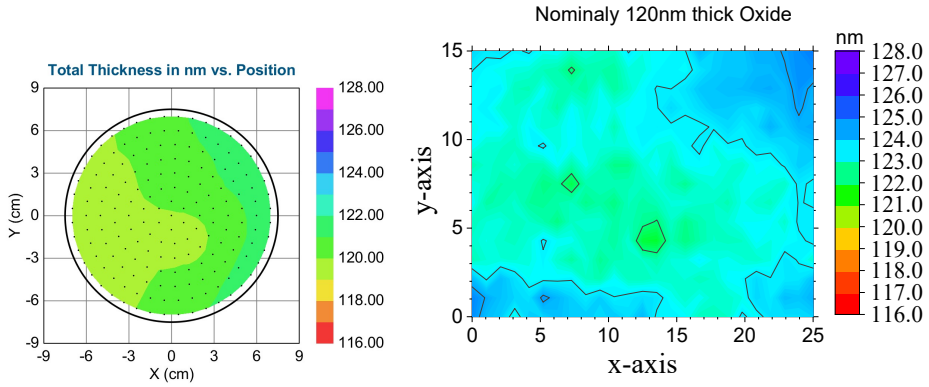

Figure 17. Thickness maps from a nominally 120 nm thick oxide film on a 20 cm diameter Si-wafer by a) Woollam M2000 ellipsometer b) our device from cheap parts. (Note that our M2000 can map only the central 14 cm diameter area of the 20 cm diameter sample.).

3.3.1 Validation using poly-Si on SiO_2 on Si samples

As a further independent test of the proposed calibration-to-analysis workflow, two polycrystalline–silicon on silicon–dioxide (poly-Si-on-SiO_2) samples were investigated. The films were deposited by standard chemical vapor deposition (CVD) on 6–inch diameter crystalline silicon wafers.

As in the previous validation on SiO_2) samples, the purpose of this experiment is not to validate the measurement itself, but to assess whether the calibration posterior obtained from reference samples can be reused consistently as an informative prior in the Bayesian analysis of more complex, multilayer structures.

The calibrated monitor–correction function $\rho_{monitor}(x,y,\lambda)$ and the angle–of–incidence map were applied to the measured RGB intensity data. Thickness maps of both the poly Si and the underlying SiO_2 layers were determined using the Bayesian inversion procedure described in the previous sections.

Independent reference measurements were performed on the same samples using a Wool lam M–2000 spectroscopic ellipsometer evaluated with the CompleteEASE software package. For both measurement systems, the same optical layer model was used, consisting of a poly–Si layer on a SiO_2 layer on a crystalline silicon substrate.

The effective dielectric function of the poly–Si layer was described by an effective–medium approximation (EMA) consisting of crystalline silicon (c–Si) and amorphous silicon (a–Si). The dielectric functions of c–Si and a–Si were taken from Ref. [16]. The amorphous–silicon fraction was determined from the spectroscopic ellipsometry (M–2000) measurements and subsequently fixed to 11% during the evaluation of the RGB ellipsometric mapping data. This choice reflects the limited information content of three broadband RGB channels and avoids introducing poorly constrained additional free parameters into the inversion.

Fig. 17 and 18 show the results. We must note that perspective causes the map to “shrink”. In both figures, the left panels correspond to the Woollam M–2000 measurements, while the right panels show the results obtained with the present RGB ellipsometric mapping system using the calibrated correction parameters. We compare the results of the point-by-point measurements and evaluation using the same optical model by the M2000 device and CompleteEASE software [15] by Woollam Co.

The two measurement systems differ fundamentally in both spectral and spatial resolution. The M–2000 measures full spectra at each point with a spot size of approximately 1 mm, whereas the present RGB system operates with three broad spectral bands and averages over pixel groups corresponding to lateral dimensions of approximately a few mm by a few mm. As a consequence, a perfect point–by–point agreement is not expected for samples exhibiting lateral thickness variations.

Nevertheless, within the overlapping measurement area, the agreement between the poly–Si thickness values obtained with the two systems is typically within approximately 1 nm. Considering the reduced spectral information content, the non–collimated illumination geometry, and the spatial averaging inherent to the RGB system, this level of agreement confirms that the calibration parameters and their associated uncertainties can be propagated consistently into the Bayesian analysis of multilayer samples.

We used the same optical model to evaluate both measurements (M2000 and our multicolor device): poly-Si(mixture of c-Si and a-Si) – SiO_2 – c-Si substrate. The poly-Si effective dielectric function was modelled by an Effective Medium Approximated (EMA) mixture of c-Si and a-Si, where c-Si (crystalline silicon) and a-Si dielectric functions were used from ref [18]. We determined the amorphous-silicon (a-Si) percentage from the M2000 measurement and we fixed this percentage (11 %) when we evaluated the imaging measurements by our multicolor device. This choice reflects the limited information content of three broadband RGB channels and avoids introducing poorly constrained additional free parameters into the inversion.

We must note, that this parameter (amorphous-silicon percentage) showed a relatively high cross-correlation with the thickness parameter and the uncertainty was ±3 % (absolute error) even in the case of the evaluation of M2000 measurements by CompleteEASE software in the same 450-650 nm wavelength range. So, our 3-colorband cannot serve enough measured data to use more sophisticated optical model. Therefore, in the present work we treat the a–Si fraction as a calibration/auxiliary input and focus the RGB evaluation on reliable thickness mapping of the multilayer structure.

To test whether three–color data can constrain the EMA composition, we performed an additional inversion in which the a–Si fraction was treated as an unknown parameter with a narrow prior centered at the M–2000 value. The resulting posterior shows strong correlation between composition and thickness parameters, indicating that RGB data provide only limited independent information on the a–Si fraction in the present configuration. However, the thickness posteriors remain stable within the valid area.

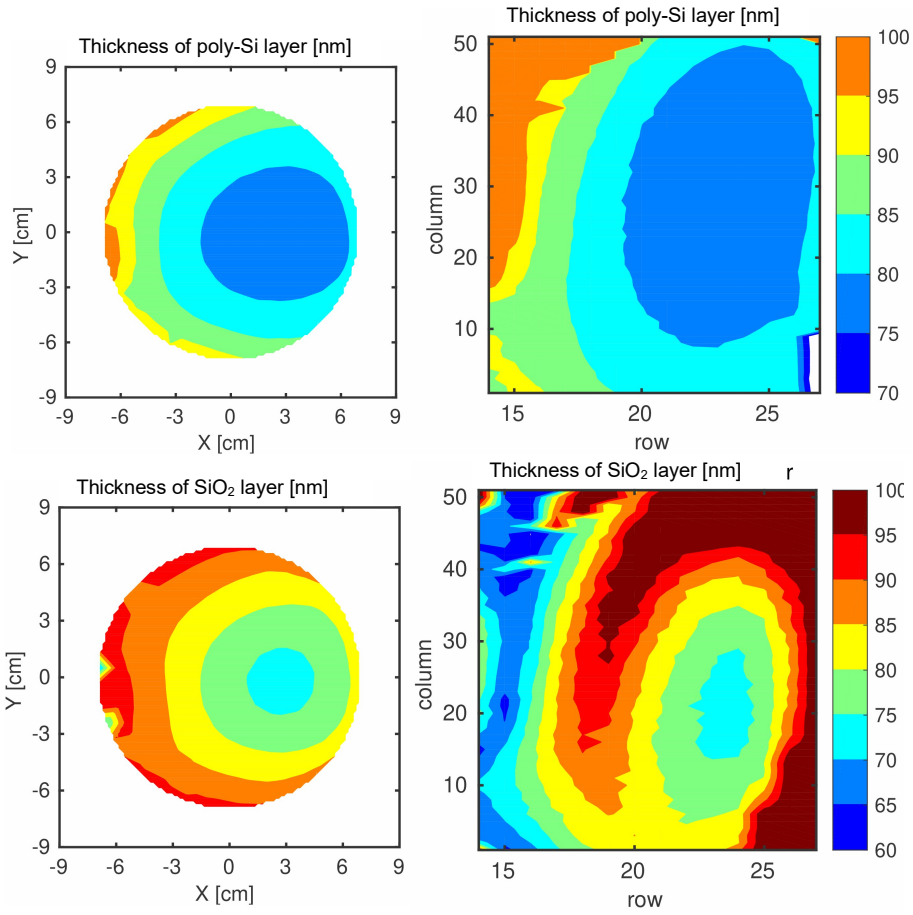

Figure 18. Thickness maps from the first poly-Si – silicon-dioxide film structure on a 6-inch diameter Si-wafer by a Woollam M2000 ellipsometer (left) or by our device from cheap parts (right). (Note that our M2000 can map only the central 14 cm diameter area of the 6 inch diameter sample.) One color is 5 nm. The full frame is: 30x30 cm, X-direction: 1-50 columns; Y-direction: 1-30 rows.

This is considered independent checking measurement of the same samples by the Woollam M2000 ellipsometer, as shown in Fig. 18 and 19. We must note that M2000 measure full spectra at each point, while our device measures at 3 color-bands. We must note that M2000 measures on 1 mm size spots, while our device averages (pixel-groups) approximately 5x5 mm spots. So, in the case of laterally changing thicknesses we cannot wait full agreement between the two measurements. The agreement between the thickness measurements made between our non-collimated ellipsometer after correction and the conventional Wollam M2000 spectroscopic ellipsometer is only within 1 nm, which is a good agreement. Note that our M2000 device can map only a 14 cm diameter area, so there isn't a one-to-one correspondence between the two areas.

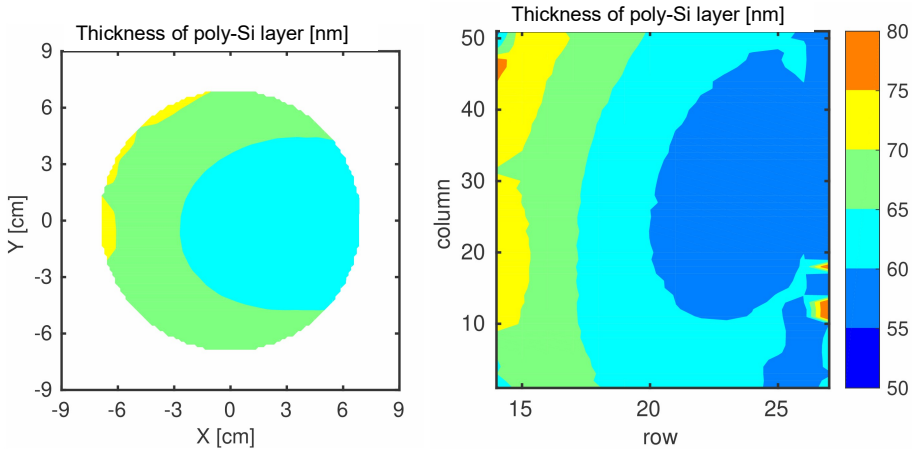

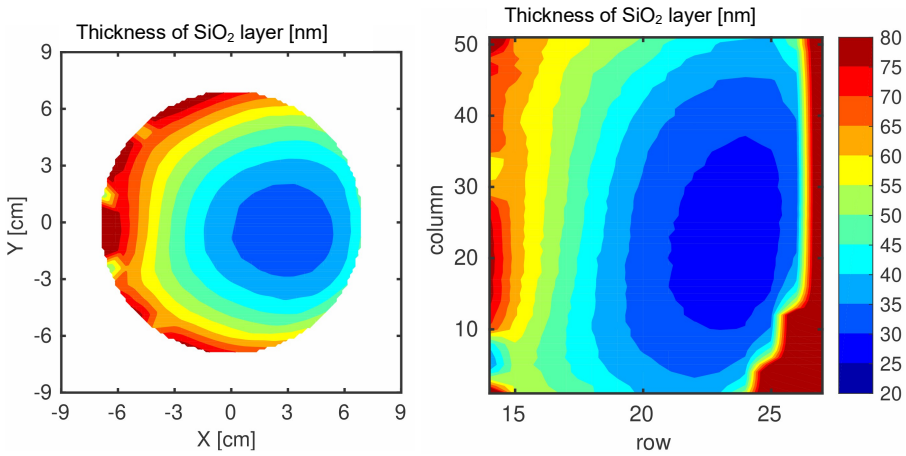

Figure 19. Thickness maps from the second poly-Si – silicon-dioxide film structure on a 6-inch diameter Si-wafer by a Woollam M2000 ellipsometer (left) or by our device from cheap parts (right). (Note that our M2000 can map only the central 14 cm diameter area of the 6 inch diameter sample.) One color is 5 nm. The full frame is: 30x30 cm, X-direction: 1-50 columns; Y-direction: 1-30 rows.

To further quantify the agreement, a comparative error analysis was performed for the second poly–Si/SiO_2/Si sample, using the device with a smaller pixel-groups. Fig. 20 and 21 show the smoothed thickness maps of fitted values of poly-Si and SiO_2 layers (left maps), the differences between the smoothed and M2000 thickness values (middle maps), and the distribution of the thickness differences.

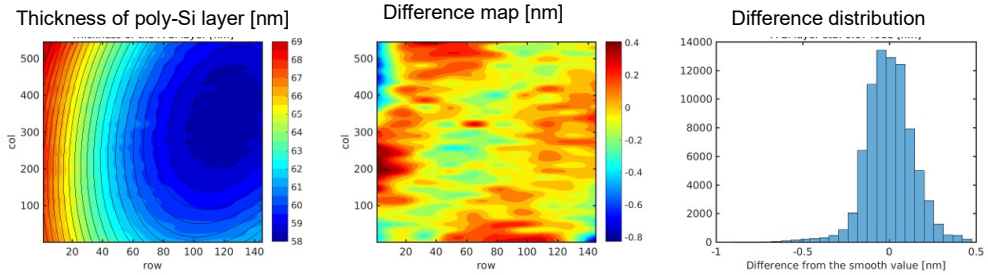

Figure 20. Smoothed thickness map of poly-Si layer (from Fig. 19); Difference of the smoothed and M2000 thickness values; Histogram of the thickness differences. One color is 0.5 nm. Here, the valid are is shown with smaller pixel-groups.

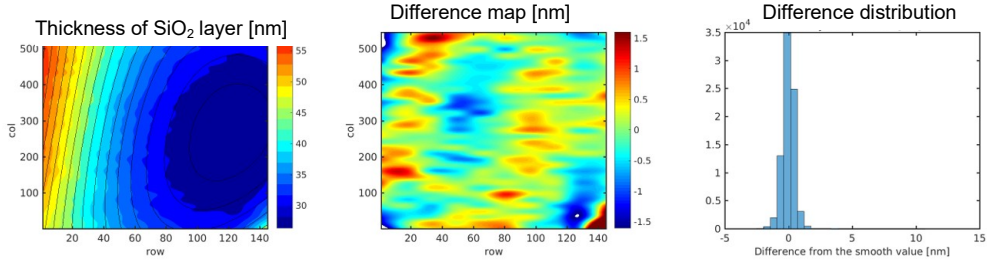

Figure 21. Smoothed thickness map of SiO_2 layer (from Fig. 19); Difference of the smoothed and M2000 thickness values; Histogram of the thickness differences. One color is 0.5 nm. Here, the valid are is shown with smaller pixel-groups.

4. Discussion

The results presented in this work demonstrate that rapid ellipsometric mapping measurements can be performed using a multi–color ellipsometric mapping instrument constructed from inexpensive, non–moving optical components. The experimental arrangement, based on a commercially available LCD monitor as a broadband polarized light source and a polarization–sensitive camera, enables large–area measurements within short acquisition times.

An important practical advantage of the proposed setup is its scalability. By employing large–format LCD panels, the measurement area can be extended to meter–scale dimensions, making the concept suitable for in–line or near–line monitoring of laterally extended samples in industrial production environments. The absence of moving optical components further supports robust and stable operation under such conditions.

The use of non–ideal and imperfect optical components, however, requires a departure from conventional ellipsometric evaluation strategies. Instead of relying on directly reconstructed tan ψ and cos Δ values, the present work employs an intensity–based forward model and a Bayesian evaluation framework. This approach allows the measured RGB intensity signals to be analyzed directly, while consistently accounting for instrumental correction parameters, measurement noise, and prior information on the sample structure.

Within this framework, Bayesian Probability Theory provides a natural and transparent way to quantify uncertainties and parameter correlations. The use of simulated annealing for global optimization ensures reliable location of the maximum a posteriori solution in a strongly non–linear and correlated parameter space. The subsequent analysis of the posterior distribution reveals not only the most probable parameter values, but also the intrinsic limitations of the measurement configuration.

A central limitation of the present approach arises from the use of only three broadband spectral channels. While this configuration is sufficient for robust thickness mapping of well–defined layer structures, it restricts the amount of independent spectral information available for simultaneously determining multiple optical parameters. This limitation manifests itself in strong posterior correlations and, in some cases, in partial parameter degeneracies. Rather than obscuring these effects, the Bayesian analysis makes them explicit and allows their impact on the inferred parameters to be assessed quantitatively.

Despite these limitations, the results show that the calibrated RGB ellipsometric mapping system, combined with a Bayesian evaluation strategy, provides reliable and quantitatively interpretable thickness maps for technologically relevant SiO_2/Si and poly–Si/SiO_2/Si structures. The method is therefore well suited for applications where fast, large–area mapping and transparent uncertainty quantification are more critical than full spectroscopic parameter reconstruction. [21]

Appendix A: Global Optimization via Simulated Annealing

The global optimization of the nonlinear inverse ellipsometry problem is performed using simulated annealing (SA) [19-21] in combination with local gradient–based refinement. Starting from an initial parameter vector x, a trial state y is generated by a random perturbation in parameter space and accepted according to the Metropolis criterion

$$P(x \to y) = min\left[e\left(\frac{-\Delta f}{T}\right), 1\right],$$

where $\Delta f = f(y) - f(x)$ denotes the change in the objective function and T is the control (temperature) parameter. At high values of T, transitions are accepted with high probability, enabling a broad exploration of the parameter space, while decreasing T progressively favors moves that reduce the objective function.

In the present Bayesian framework, the objective function f corresponds to the negative logarithm of the posterior probability (up to an additive constant). Consequently, the simulated annealing procedure performs a global search for the maximum of the posterior distribution, yielding a maximum a posteriori (MAP) estimate of the model parameters.

Although it can be shown that simulated annealing converges to the global optimum for sufficiently slow cooling schedules, such schedules are computationally impractical for high–dimensional parameter spaces. To improve efficiency, the SA search is therefore combined with a local gradient–based optimization using the Levenberg–Marquardt (LM) algorithm. Once the SA procedure identifies a promising region in parameter space, LM refinement is applied to rapidly converge to the nearest local minimum of the objective function.

To further enhance robustness against trapping in suboptimal local minima, a reannealing strategy is employed. If convergence stagnates, the temperature is temporarily increased and the SA search is restarted, allowing the algorithm to escape local minima and resume global exploration. This hybrid SA+LM approach provides a reliable compromise between global optimality and computational efficiency.

The described optimization strategy is applied consistently to both the calibration stage and the analysis of unknown multilayer samples, ensuring robust parameter estimation in the presence of strong nonlinearities and complex parameter correlations.

Appendix B: Robustness of the Bayesian Calibration

The simulated calibration data were generated using reference SiO_2/Si samples with oxide thicknesses of 60 nm, 80 nm, 100 nm, and 120 nm. For two calibration samples, the 60 nm and 80 nm wafers were used; for three samples, the 60 nm, 80 nm, and 100 nm wafers were included; and for four samples, all four thicknesses were employed.

Table I summarizes the resulting posterior standard deviations of the calibration parameters as a function of the number of calibration samples (NoS). The rows correspond to the number of samples, while the columns list the absolute uncertainties of the angle-of-incidence parameter and of the monitor-correction parameters.

Table 1: Posterior standard deviations of the calibration parameters as a function of the number of calibration samples (NoS). The table lists the absolute uncertainties of the angle-of-incidence parameter θ and of the monitor-correction parameters ρ (magnitude and phase) for the blue (B), green (G), and red (R) channels. The systematic reduction of posterior uncertainties with increasing NoS demonstrates the robustness of the Bayesian calibration procedure.

NoS	σ_θ	$\sigma \lvert\rho\rvert_B$	$\sigma \lvert\rho\rvert_G$	$\sigma \lvert\rho\rvert_R$	$\sigma \arg(\rho)_B$	$\sigma \arg(\rho)_G$	$\sigma \arg(\rho)_R$
2	2.2976	0.0352	0.0303	0.0341	0.1649	0.1637	0.1772
3	0.2469	0.0301	0.0229	0.0178	0.0209	0.0229	0.0226
4	0.1266	0.0185	0.0183	0.0124	0.0113	0.0162	0.0143

Acknowledgments: Authors thank the support from the National Development Agency grant OTKA K 143216 and 146181 projects, and TKP2021-EGA-04 project from the Ministry of Innovation and Technology of Hungary from the National Research, Development and Innovation Fund.

References

1. R. M. A. Azzam, and N. M. Bashara, "*Ellipsometry and Polarized Light*"; Elsevier: Amsterdam, 1977
2. H. Fujiwara, "*Spectroscopic Ellipsometry: Principles and Applications*"; Wiley, Tokyo, 2007
3. Harland G. Tomkins, and Eugene A. Irene, "*Handbook of Ellipsometry*"; Springer-Verlag, Berlin and Heidelberg, 2004
4. Maria Losurdo & Kurt Hingerl (Eds), "*Ellipsometry at the Nanoscale*", Springer, 2013
5. Martin Pincus, Letter to the Editor—A Monte Carlo Method for the Approximate Solution of Certain Types of Constrained Optimization Problems. *Operations Research* **1970** *18(6)*: 1225-1228., https://doi.org/10.1287/opre.18.6.1225
6. Kirkpatrick, S.; Gelatt Jr, C. D.; Vecchi, M. P. Optimization by Simulated Annealing, *Science* **1983** *220* 671–680. doi:10.1126/science.220.4598.671
7. Polgar, O.; Fried, M.; Lohner, T.; Barsony, I., Comparison of algorithms used for evaluation of ellipsometric measurements: Random search, genetic algorithms, simulated annealing and hill climbing graph-searches, *SURFACE SCIENCE* **2000** *457* pp. 157-177
8. Zereay, B.N.; Kálvin, S.; Juhász, G.; Major, C.; Petrik, P.; Horváth, Z.G.; Fried, M. Optical Calibration of a Multi-Color Ellipsometric Mapping Tool Fabricated Using Cheap Parts. *Photonics* **2024** *11* 1036. https://doi.org/10.3390/photonics11111036
9. Sivia, D S, Data Analysis: A Bayesian Tutorial (Oxford, 2006; online edn, Oxford Academic, 31 Oct. 2023), https://doi.org/10.1093/oso/9780198568315.001.0001, accessed 3 Dec. 2025.
10. Gregory P., Bayesian Logical Data Analysis for the Physical Sciences: A Comparative Approach with Mathematica® Support., Cambridge University Press, September 2012, ISBN: 9780511791277, https://doi.org/10.1017/CBO9780511791277
11. Barradas N.P., Keddie J.L., Sackin R., Bayesian inference analysis of ellipsometry data. *Phys Rev E* **1999** *59*, 6138-51, doi: 10.1103/physreve.59.6138
12. Udo v. Toussaint and V. Dose, Bayesian Inference in Surface Physics, *Appl. Phys. A* **2006** *82* pp. 403-413

13. https://semilab.com/hu/product/799/fpt, accessed 2025-10-28
14. https://www.jawoollam.com/download/pdfs/accumap-se-brochure.pdf, accessed 2025-10-28
15. https://www.jawoollam.com/ellipsometry-software/completeease, accessed 2025-10-28
16. G. E. Jellison, Use of the biased estimator in the interpretation of spectroscopic ellipsometry data, *Appl. Opt*. **1991** *30(23)*, 3354–3360
17. Lester Ingber *Adaptive simulated annealing (ASA): Lessons learned*, arXiv:cs.MS/0001018 23 Jan 2000, Journal reference: Control and Cybernetics **1996** *25* 33-54
18. E.D. Palik (Ed.) *Handbook of Optical Constants of Solids*, Academic Press, Orlando, **1985**
19. S. Kirkpatrick, C. D. Gelatt, and M. P. Vecchi, Optimization by simulated annealing, Science **1983** *220* 671–680
20. E. Aarts and J. Korst, Simulated Annealing and Boltzmann Machines: A Stochastic Approach to Combinatorial Optimization and Neural Computing, Wiley, Chichester, **1989**
21. Sándor Kálvin, Berhane N. Zereay, György Juhász, Csaba Major, Péter Petrik, Zoltán György Horváth, Miklós Fried, "A new method to evaluate multi-color ellipsometric mapping on big area samples", Sci 8(1), p. 17 (2026) https://doi.org/10.3390/sci8010017

Validity of Young-Dupré equation for advancing and receding situations by the Capillary Bridge Probe method

Norbert Nagy[1]

[1]HUN-REN Centre for Energy Research, Institute of Technical Physics and Materials Science,

1121 Budapest, Konkoly-Thege Miklós út 29–33.

nagy.norbert@ek.hun-ren.hu

The need for the determination of solid-liquid adhesion work is as old as Dupré's definition of the reversible work of adhesion. In addition to its scientific importance, this quantity is a critical factor affecting product quality and performance in many industrial fields. In general, it plays crucial role if the liquid should completely cover a solid surface (e.g. coatings, paints, inks, lubricants, adhesives, pesticides) or, on the contrary, the liquid should not remain on the surface at all (liquid repellency, anti-icing, etc.).

Previously, a novel method was introduced to determine the value of adhesion work on flat surfaces directly, without the need of any model assumptions, and independently from uncertainties of contact angles. The presented method enables us to determine the adhesion work separately both for advancing and receding situations.

During a measurement cycle of capillary bridge probe, the capillary force is measured as a function of the change of bridge length that is as a function of the vertical displacement of the cylinder.

This work is only spent on changing the interfacial areas, if gravitational force is negligible. During approach and retraction, both the area of the liquid-vapor interface (A) and that of the solid-liquid interface (B) change. Consequently, the energy balance can be written as

$$-\int \vec{F}\,d\vec{z} = \Delta A \cdot \gamma_{LV} + \Delta B \cdot (\gamma_{SL} - \gamma_{SV}) \qquad (1)$$

where $\vec{F}$ is the measured capillary force, $\vec{z}$ is the displacement of the cylinder, ΔA is the change of interfacial area between the liquid and vapor phase, and ΔB is the area change between the solid and the liquid, see Fig. 1. (The value of ΔA and ΔB are also dependent on the start and end points of the interval (z-range), over which the integration is performed.)

After rearranging Equation (1), the difference term in the bracket can be expressed as:

$$(\gamma_{SL} - \gamma_{SV}) = -\frac{\int F \, d\vec{z} + \Delta A \cdot \gamma_{LV}}{\Delta B}. \quad (2)$$

One can substitute this experimentally otherwise unattainable term into the definition of adhesion work:

$$W_a \equiv \gamma_{LV} - (\gamma_{SL} - \gamma_{SV}) \quad (3)$$

Furthermore, considering that the net force and the displacement have only z-component, the vector notation can be omitted. This resulting formula gives the value of the solid-liquid adhesion work without the need of including any contact angle in the equation:

$$W_a = \gamma_{LV} + \frac{\int F \, dz + \Delta A \cdot \gamma_{LV}}{\Delta B}. \quad (4)$$

Integration between the start and end points of approach and retraction gives the mechanical work done in the advancing and receding phases, respectively. The change of interfacial areas can be determined by simple image analysis in cylindrically symmetric case. Therefore, the solid-liquid adhesion work can be calculated according to Equation (6) for both the advancing and receding contact lines.

It is an interesting question what is the relation between the directly measured adhesion work values and the values calculated from the Young-Dupré equation? In other words: is the Young-Dupré equation valid separately for advancing and receding situations? In Figure 1, the directly measured adhesion work values were plotted. The blue and red points represent the work of adhesion measured in the advancing and receding phase, respectively. The green points were measured in readvancing situation. This readvancing effect can be observed in case of perfect wetting: the receding contact line starts to advance again during the retraction of the cylinder. (The readvancing contact line already finds wetted surface in front of it, hence the measured contact angle is lower than in the receding situation, its value is typically ≤1°.) The corresponding vertical error bars show the standard deviation of the directly measured adhesion work values determined according to the above-described procedure. The adhesion work values were plotted as a function of contact angle, of which values were measured during the same capillary bridge probe measurement and obtained by analytic evaluation as described previously. The horizontal error bars show their standard deviation.

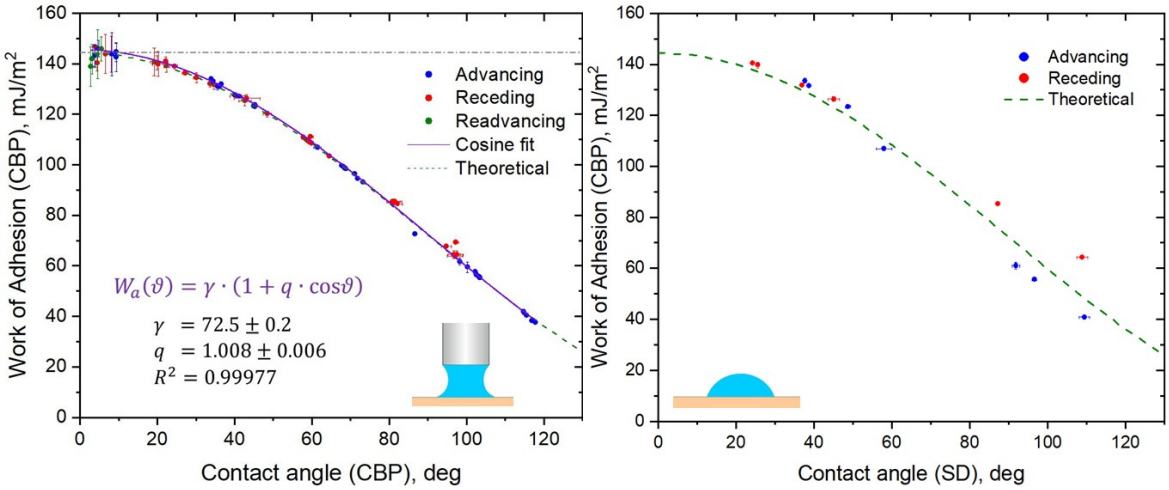

Figure 1: (*left*) Directly measured adhesion work values as a function of contact angles determined during the same capillary bridge probe (CBP) measurement. The inset shows the result of the fit of a general cosine function to all measurement points. The fitted purple curve is in excellent agreement with the theoretical dashed green curve corresponding to the Young–Dupré equation. For this validation, metal, semiconductor, dielectric, and polymer surfaces were measured in clean, contaminated, acid-, and plasma-treated condition using ultrapure water as test liquid. (*right*) Work of adhesion values measured by capillary bridge probe (CBP) as a function of water contact angles determined by the sessile drop (SD) method. The purple dashed line represents the theoretical prediction of the Young–Dupré equation.

In conclusion, accurately measured advancing and receding contact angles can be used to calculate the adhesion work for the two different situations. It is worth to note that the calculation of adhesion work from the Young–Dupré equation relies on the precise measurement of the contact angle. When for instance, the directly measured adhesion work is plotted against the sessile drop contact angles, the correlation is of much lower quality (Figure 1 (right)). Furthermore, in accordance with the previous consequence, this novel direct method provides an additional advantage: if the receding contact angle is not a stationary definite value, an effective receding contact angle can be calculated from the measured adhesion work using the Young–Dupré equation.

References

[10] N. Nagy "Determination of solid-liquid adhesion work on flat surfaces in a direct and absolute manner" *Scientific Reports*, 14:29991 2024. [https://doi.org/10.1038/s41598-024-81710-6]

[11] N. Nagy „Eljárás és berendezés folyadék-szilárd adhéziós munka meghatározására" *Hungarian patent* (231 506)

[12] N. Nagy „Method and Apparatus for Determining Liquid-Solid Adhesion Work", *WIPO PCT patent application* (WO2023094846) [https://patentscope.wipo.int/search/en/detail.jsf?docId=WO2023094846]